NASA CR-174623

Contract NAS7-918
Task Order RE-65, Amendment 399

Test Bed Ion Engine Development

Final Report

By
Graeme Aston
William D. Deininger
Electric Propulsion and Plasma
Technology Group
Jet Propulsion Laboratory
California Institute of Technology
Pasadena, California

March 1984

Prepared for

National Aeronautics and Space Administration
NASA Lewis Research Center
Vincent K. Rawlin, Program Manager

1 Report No	2 Government Accession No	3 Recipient's Catalog No
CR-174623		

4 Title and Subtitle	5 Report Date
Test Bed Ion Engine Development	March, 1984
	6 Performing Organization Code

7. Author(s)	8. Performing Organization Report No
Graeme Aston, William D. Deininger	
	10 Work Unit No

9 Performing Organization Name and Address	11 Contract or Grant No
Jet Propulsion Laboratory 4800 Oak Grove Drive Pasadena, CA 91109	NAS7-918
	13. Type of Report and Period Covered Final Report Sept. 1982 - Nov. 1983
12 Sponsoring Agency Name and Address	14 Sponsoring Agency Code
NASA Lewis Research Center 21000 Brookpark Rd. Cleveland, OH 44135	

15. Supplementary Notes

Program Manager: Vincent K. Rawlin,
NASA Lewis Research Center,
Cleveland, OH 44135

16 Abstract

A Test Bed Ion (TBI) engine has been developed to serve as a tool in exploring the limits of electrostatic ion thruster performance. This report describes three key ion engine components, the Decoupled Extraction and Amplified Current (DE-AC) accelerator system, Field Enhanced Refractory Metal (FERM) hollow cathode and Divergent Line Cusp (DLC) discharge chamber, whose designs and operating philosophies differ markedly from conventional thruster technology. Significant program achievements were: high current density DE-AC accelerator system operation at low electric field stress with indicated feasibility of a 60 mA/cm^2 argon ion beam, reliable FERM cathode start up times of 1-2 secs. and demonstrated 35 ampere emission levels, DLC discharge chamber plasma potentials negative of anode potential and identification of an efficient high plasma density engine operating mode. Using the performance projections of this program and reasonable estimates of other parameter values, a 1.0 newton thrust ion engine is identified as a realizable technology goal. Calculations show that such an engine, comparable in beam area to a J series 30 cm thruster, could, operating on X_e or H_g, have thruster efficiencies as high as 0.76 and 0.78, respectively, with a 100 eV/ion discharge loss.

17. Key Words (Suggested by Author(s))	18 Distribution Statement
Ion Engine Accelerator System Hollow Cathode Discharge Chamber	Unclassified - Unlimited

19 Security Classif (of this report)	20. Security Classif (of this page)	21. No. of Pages	22 Price*
Unclassified	Unclassified		

* For sale by the National Technical Information Service, Springfield, Virginia 22161

ACKNOWLEDGMENT

The work presented in this report was performed at the Jet Propulsion Laboratory by members of the Electric Propulsion and Plasma Technology Group. Those group members who made major contributions during the conduct of the program were, Allison Owens, Robert Toomath and Lewis Pless. Their efforts and those of others in the group, who offered many valuable suggestions during the preparation of this report, are recognized herein.

Graeme Aston

Supervisor

Electric Propulsion and

Plasma Technology Group

CONTENTS

CONTENTS Contd.

LIST OF FIGURES

LIST OF FIGURES Contd.

LIST OF TABLES

NOMENCLATURE

d_s	screen grid hole diameter, mm
d_f	focusing grid hole diameter, mm
d_a	accelerator slot width, mm
d_d	decelerator slot width, mm
E_e	extraction gap field stress, V/mm
e	electronic charge, coul.
g	gravitational acceleration, m/sec^2
I_{sp}	specific impulse, sec
J_D	discharge current, ampere
j_A	amplified Child's law current density, mA/cm^2
j_{AO}	normal Child's law current density, mA/cm^2
j_e	extracted current density, mA/cm^2
J_B	beam current, ampere
ℓ_e	extraction gap length, mm
ℓ_a	acceleration gap length, mm
ℓ_d	deceleration gap length, mm
ℓ	accelerated ion position, mm
m	ion mass, kg
$\dot{m}$	propellant mass flow rate, sccm
n_m	Maxwellian electron number density, m^{-3}
P_o	stagnation pressure, Torr
P	total thruster input power, watt
R	net-to-total voltage ratio
R_s	screen grid radius of curvature, mm
t_s	screen grid thickness, mm

t_f	focusing grid thickness, mm
t_a	accelerator electrode diameter, mm
t_d	decelerator electrode diameter, mm
T_m	Maxwellian electron temperature, eV
T	ion engine thrust, newton
V_s	screen grid voltage, volt
V_f	focusing grid voltage, volt
V_A	accelerator electrode voltage, kV
V_d	decelerator electrode voltage, volt
V_D	discharge voltage, volt
V_1	extraction gap voltage, volt
V_2	post acceleration voltage, volt
V_{NC}	neutralizer coupling voltage, volt
V_{MC}	mask-to-cathode voltage, volt
V_P	plasma potential relative to emitter tube, volt
V_c	cathode body potential, volt
V	accelerated ion voltage, volt
v	ion velocity, m/sec
W	DE-AC module width, mm
X	axial position from screen grid, cm
ε_o	vacuum permitivity, farad/m
ε	discharge loss, eV/ion
ρ	charge density, coul./m^3
η_u	propellant utilization

NOMENCLATURE Contd.

η_T	ion engine efficiency
γ	beam divergence and double ion loss factor
$\emptyset$	electronic work function, eV

SECTION 1

INTRODUCTION

Development of high thrust density ion engines is an increasingly important technology need as more energetic and reduced trip time electric propulsion missions are considered. Specific impulse mission constraints usually impose an upper limit to the ion beam energy, leaving increased beam current density as the desired approach to raising ion engine thrust density. This beam current increase can be achieved by making the discharge chamber plasma density profile more uniform so that more ions are available for extraction. Presently, ion thruster discharge chambers have relatively peaked plasma flatness parameters in the range 0.45-0.55. In addition, beam current can, in principle, be further increased by raising the accelerator system electric field stress. However, present ion thruster grid system designs generally cannot be operated at field stresses approaching their breakdown limit. This results from mechanical considerations which dont allow such close electrode spacings over the relatively large thruster diameters. As a consequence of these restrictions, there is an upper limit to the beam current that can be extracted with these accelerator systems.

This report presents the results of a technology development program to significantly increase ion engine thrust density. The major motivation for this work was the recent development of an ion accelerator system which showed the capability for high beam current density ion engine operation.[1] While originally initiated as an accelerator system investigation, the program was expanded to include testing of an oxide-free metallic emitter hollow cathode and a divergent line cusp discharge chamber. These latter components were developed as a working plasma source to provide

very high ion flux levels for the accelerator system beam extraction tests. However, discharge chamber performance was so encouraging as to warrant the eventual construction of a Test Bed Ion (TBI) engine incorporating the accelerator system, divergent line cusp plasma containment scheme and metallic emitter hollow cathode. It is this TBI engine, a description of its component technologies and its application to testing the limits of high thrust density operation, that comprises this report.

SECTION 2

PRINCIPLES OF OPERATION

This section discusses the theoretical basis and operating principles of the Decoupled Extraction and Amplified Current (DE-AC) accelerator system, the Field Enhanced Refractory Metal (FERM) hollow cathode and the Divergent Line Cusp (DLC) discharge chamber.

2.1 DE-AC ACCELERATOR SYSTEM

As the name implies, the DE-AC ion optical system separates the ion extraction process from the acceleration and focusing processes. This separation of functions results in much higher beam current densities, at the same electric field stress, when compared to conventional ion thruster accelerator systems.

2.1.1 Ion Extraction Limits

During operation of an ion thruster extraction system the indication a beam current limit has been reached is sudden and direct accelerator grid ion impingement. This impingement results from space charge forces between the ions overcoming the externally imposed electric fields which guide their motion. However, it is possible to rearrange the imposed field distribution so that this beam blow up and subsequent impingement occurs at larger ion current densities. With a conventional ion thruster grid set this effect may be observed by increasing the net-to-total accelerating voltage ratio, R, while holding the total voltage, V_T, constant. Under these conditions it has been shown that the impingement limited beam current

increases.[2,3] This phenomenon is depicted in Fig. 1. For any value of R less than 1.0 the diverging electric fields in the deceleration region act to enhance space charge blow up of the ion beamlet in the vicinity of the accelerator aperture. At low R values this enhancement is great (Fig. 1a) but decreases as R approaches 1.0 (Fig. 1b). However, for R >1.0 an abrupt change occurs. The downstream electric fields further accelerate the ions and impart forces that neck down the beam (Fig. 1c) preventing impingement. In practice, conventional ion thruster grid sets experience electron backstreaming at R ~ 0.9. Indeed, by definition, operation at R >1.0 for these grid sets is impossible.

2.1.2 Design Features

The DE-AC accelerator system shown in Fig. 2 operates with its first, or ion extraction stage, at R >1.0. This is possible because the ions are post accelerated as they leave the focusing electrode. In the second, or acceleration and focusing stage, the ion beamlets from the multiple hole extraction stage are brought to a common focus within the large slotted accelerator electrode. Beyond the accelerator electrode these ions enter the third, or decelerator stage, where they are returned to ground potential. Injecting ions with large initial velocities into the acceleration stage significantly increases the influence of the externally imposed electric fields on ion motion within this stage. The space charge beam current limit of the acceleration stage is thereby increased and is described by a modified Child's law current density expression which is derived in Appendix A and which has the following form:

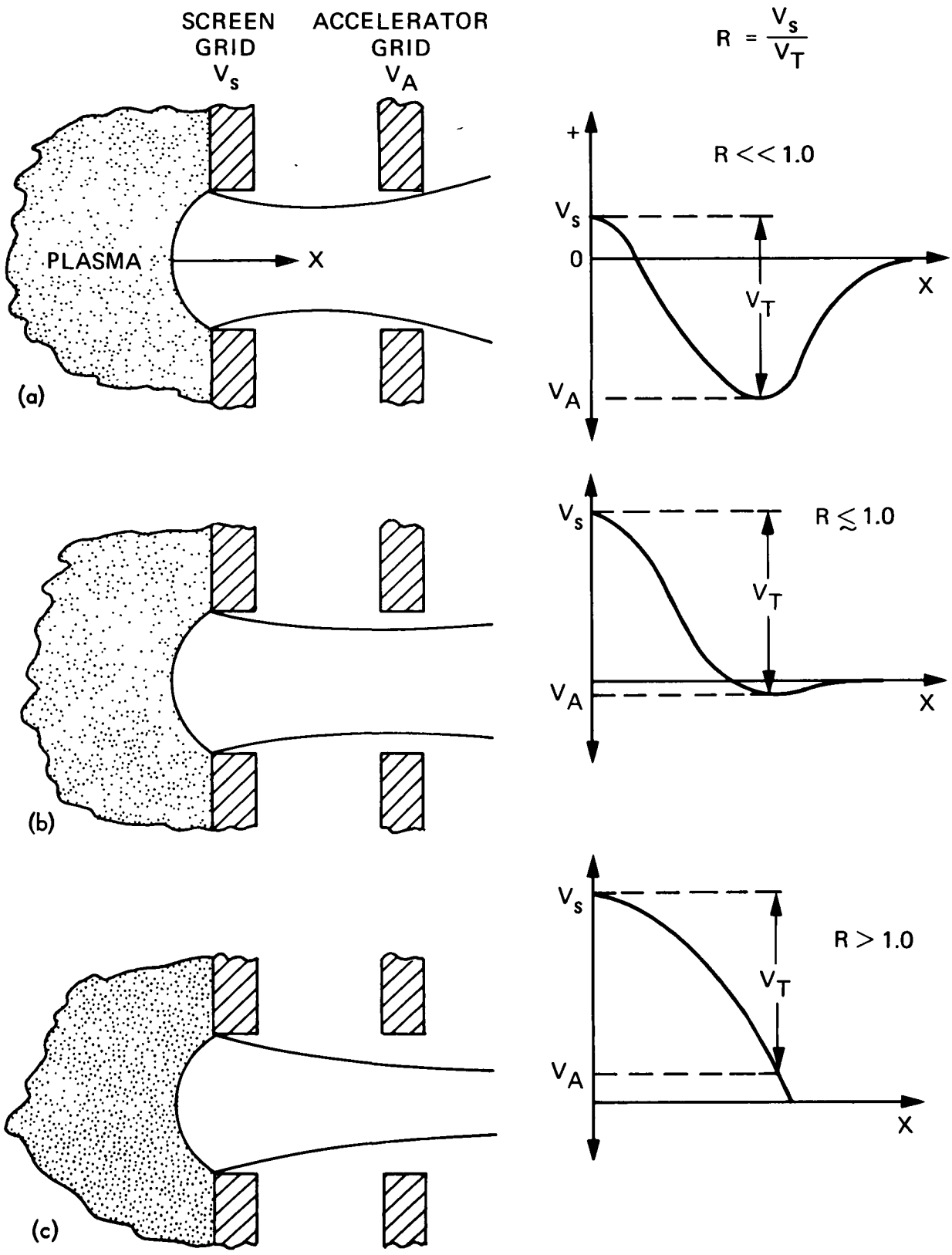

Fig. 1. Effect of R on Beamlet Shape

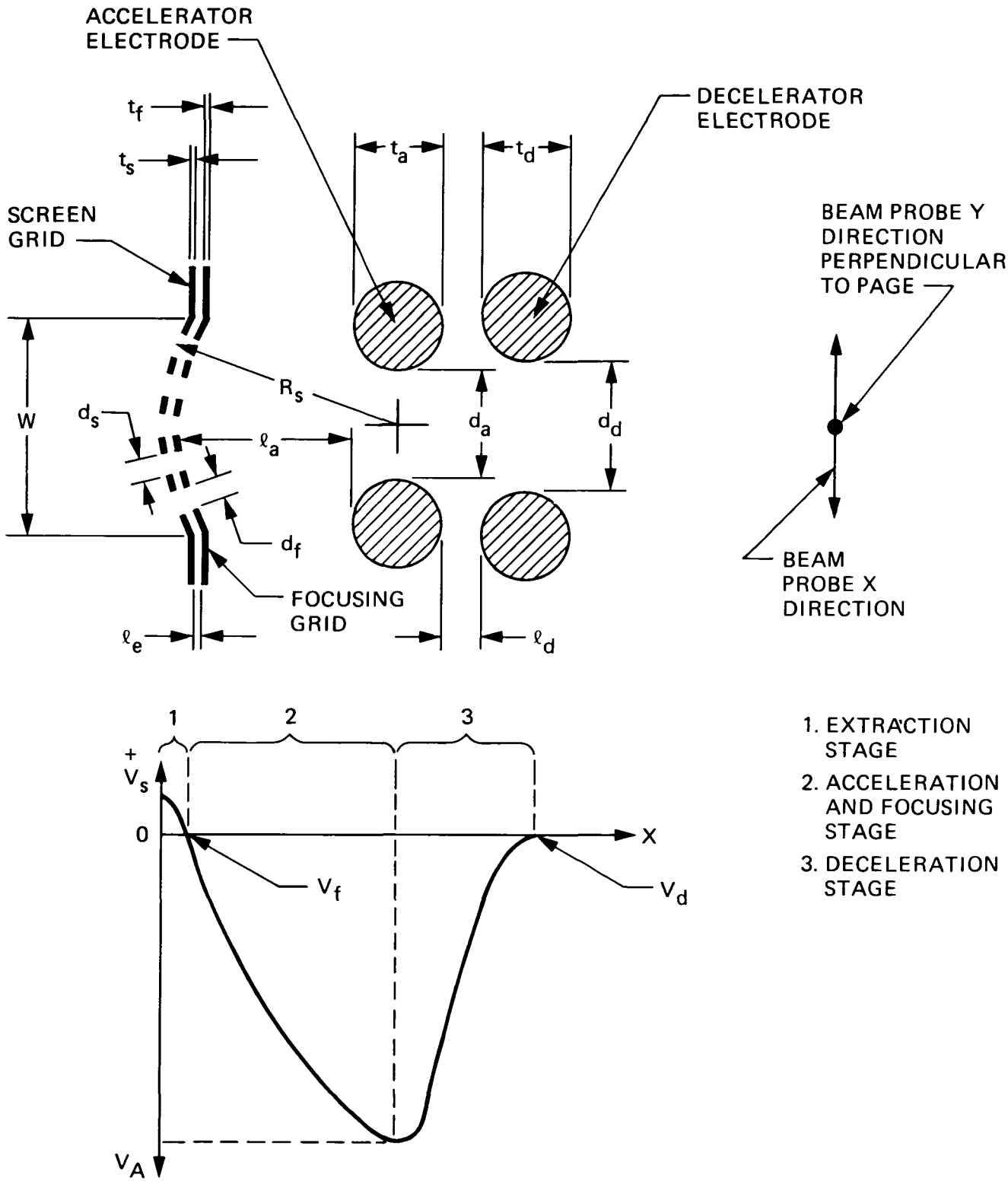

Fig. 2. DE-AC Accelerator System Design

$$\frac{j_A}{j_{AO}} = \frac{\left(\left(\frac{V_2}{V_1}\right)^{\frac{1}{2}} - 1\right)\left(\left(\frac{V_2}{V_1}\right)^{\frac{1}{2}} + 2\right)^2}{\left(\frac{V_2}{V_1}\right)^{\frac{3}{2}}} \quad . \qquad 1$$

The quantity j_A/j_{AO} is the ratio of current density for a non-zero initial ion velocity to the normal Child's law current density with zero initial ion velocity. Here, V_1 is the injected ion energy in eV and V_2 the final ion energy, in eV, after post acceleration. Appendix A defines V_1 and V_2 in terms of DE-AC accelerator system electrode potentials. Figure 3 shows a plot of j_A/j_{AO} as a function of the acceleration-to-extraction gap voltage ratio V_2/V_1. Hence, in the DE-AC accelerator system, where typically $V_2/V_1 \sim 10$, the current density capability of the accelerator stage is typically enhanced by a factor of 1.8 because of the pre-accelerated ions injected from the extraction stage. Consequently, a greater flux of ions can pass through this stage before their own space charge significantly affects the externally imposed fields guiding their motion. A further advantage of this arrangement is that the accelerator and decelerator electrodes are quite large and so can easily be shaped to minimize direct ion interception. This latter capability is especially important for the decelerator electrode because the slowed ions have a high number density and significant ion space charge as they pass through this electrode.

2.1.3 Electrode Biasing Configurations

The DE-AC accelerator system, as shown in Fig. 2, has both the focusing and decelerator grids grounded and therefore requires only two power

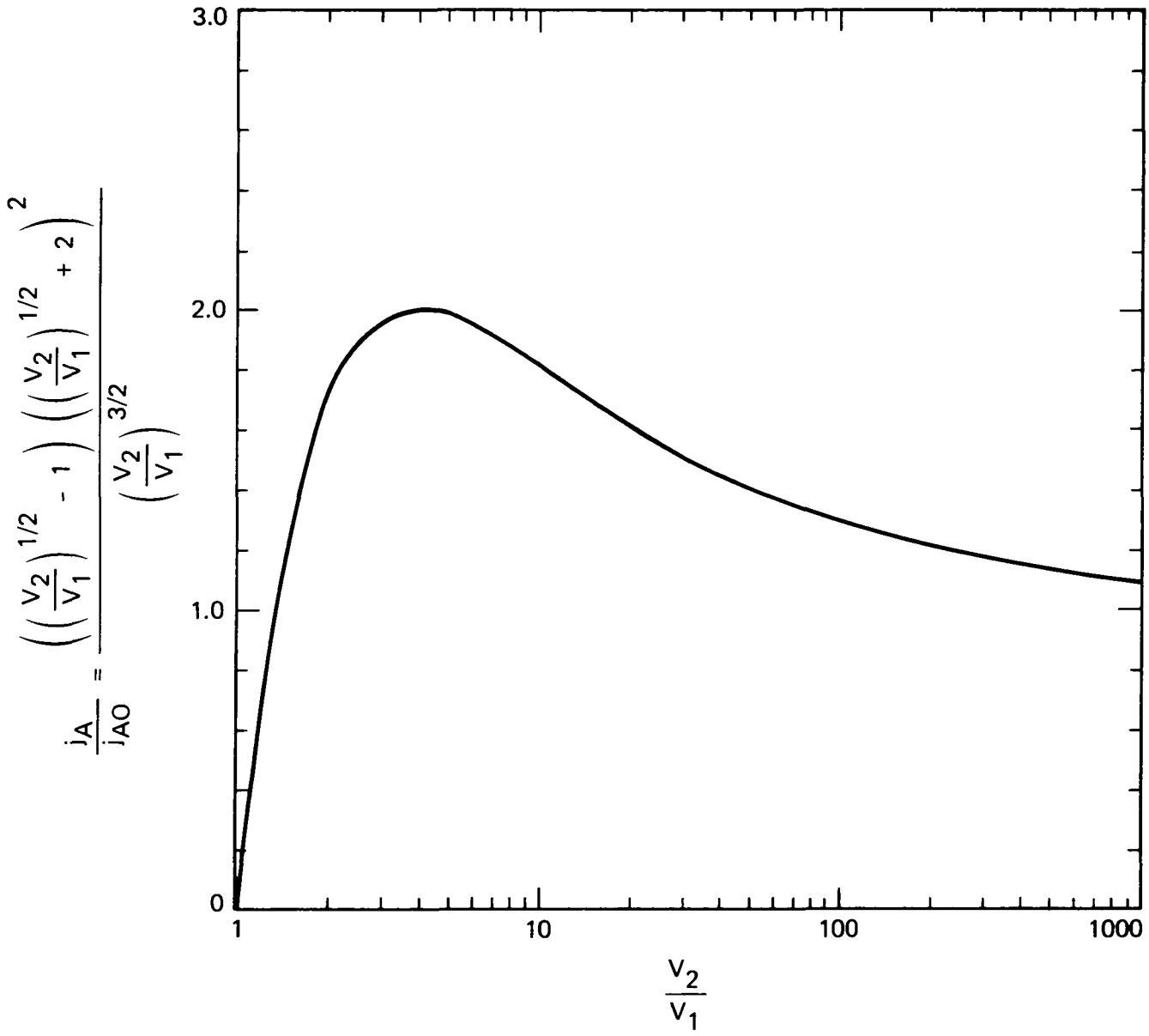

Fig. 3. Effect of Initial Ion Velocity on Child's Law Current Density

supplies. This system represents the simplest arrangement and was used throughout this test program. The specific impulse range possible with this biasing configuration is limited because the screen grid potential, when added to the discharge plasma potential, determines beam energy. However, with the addition of a focusing grid power supply, the DE-AC accelerator system can, in principle, be operated over a much wider specific impulse range as is shown in Fig. 4. With this more general biasing arrangement, independent control of specific impulse from 1500 to 25000 secs. (for argon) is possible at any beam current level, with no accelerator system geometry changes. The low specific impulse limit is reached when the screen grid potential equals the discharge plasma potential, while insulator size and X-ray generation considerations help define the practical upper specific impulse limit.

To specify perveance, for the DE-AC accelerator system, only the extraction stage potential difference and beam current are used. This is so because the potentials from the far removed accelerator or decelerator electrodes cannot reach back through the closely coupled extraction stage grids to significantly affect the ion engine discharge plasma. Such behavior is different from conventional two or three-grid ion thruster accelerator systems where ion extraction and acceleration occurs within a common gap defined by the screen hole plasma sheath and accelerator grid.

2.2 FERM HOLLOW CATHODE

Ion thruster hollow cathodes presently employ oxide impregnated porous tungsten inserts as the electron emitting structure. These cathodes have demonstrated very long life (tens of thousands of hours), are well understood and can be scaled to small and large power levels. However, by the nature of their design, these cathodes do have certain operating limitations.

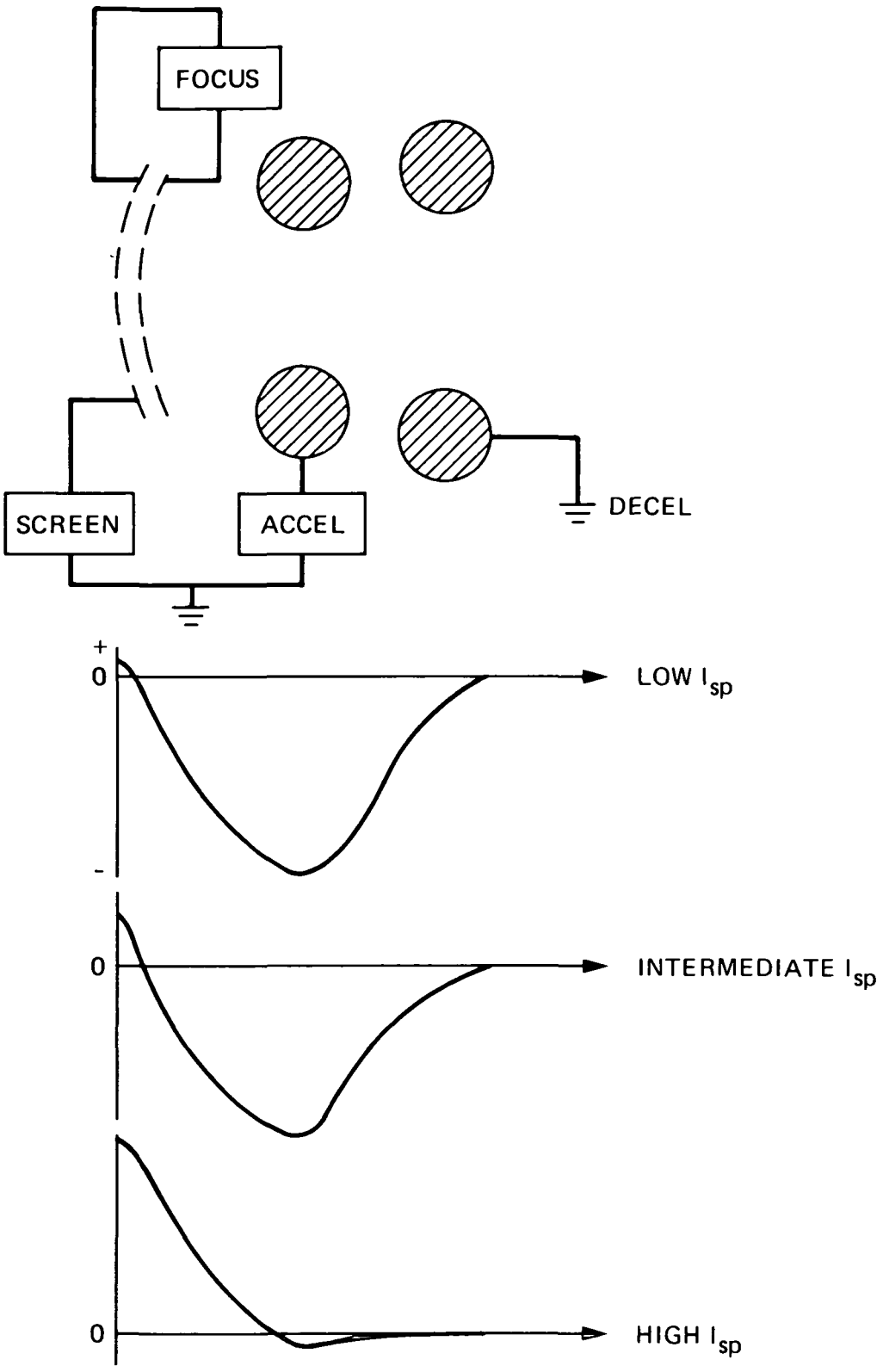

Fig. 4. DE-AC Accelerator System Biasing Configurations

Start up times are generally of the order of several minutes with arc ignition by a random keeper coupling process or by drawing a spark from an external tickler electrode. Additionally, present ion thruster cathodes are fairly complex devices requiring several carefully manufactured parts. In particular, careful monitoring of the insert manufacturing and oxide inpregnation processes is required to ensure repeatable cathode operating characteristics.

2.2.1 Design and Operating Features

The Field Enhanced Refractory Metal (FERM) hollow cathode was developed as an alternative to conventional oxide hollow cathodes and exhibits unique design and operating characteristics which make it attractive for ion thruster applications. Figure 5 shows the FERM cathode design developed for and tested with the TBI engine. No insert or resistance heaters are used with the device. Instead, a voltage, applied between the central emitter tube and surrounding cathode barrel, breaks down the injected propellant gas to form a glow discharge. This glow discharge rapidly heats the emitter tube end to thermionic electron emitting temperatures. The much larger heat capacity of the cathode barrel prevents this component from heating significantly during the starting process. When the emitter tube begins emitting thermionically, a rapid transition from a glow to an arc discharge occurs, resulting in a low coupling voltage between the emitter tube and surrounding cathode barrel. Once this arc is established the cathode is on and is a stable, high density plasma, electron source. To extract these electrons requires only a few tens of volts positive bias on the ion engine discharge chamber anode.

Figure 6 shows typical volt-ampere starting characteristics for the FERM cathode shown in Fig. 5. The 1-2 second starting times depend primarily

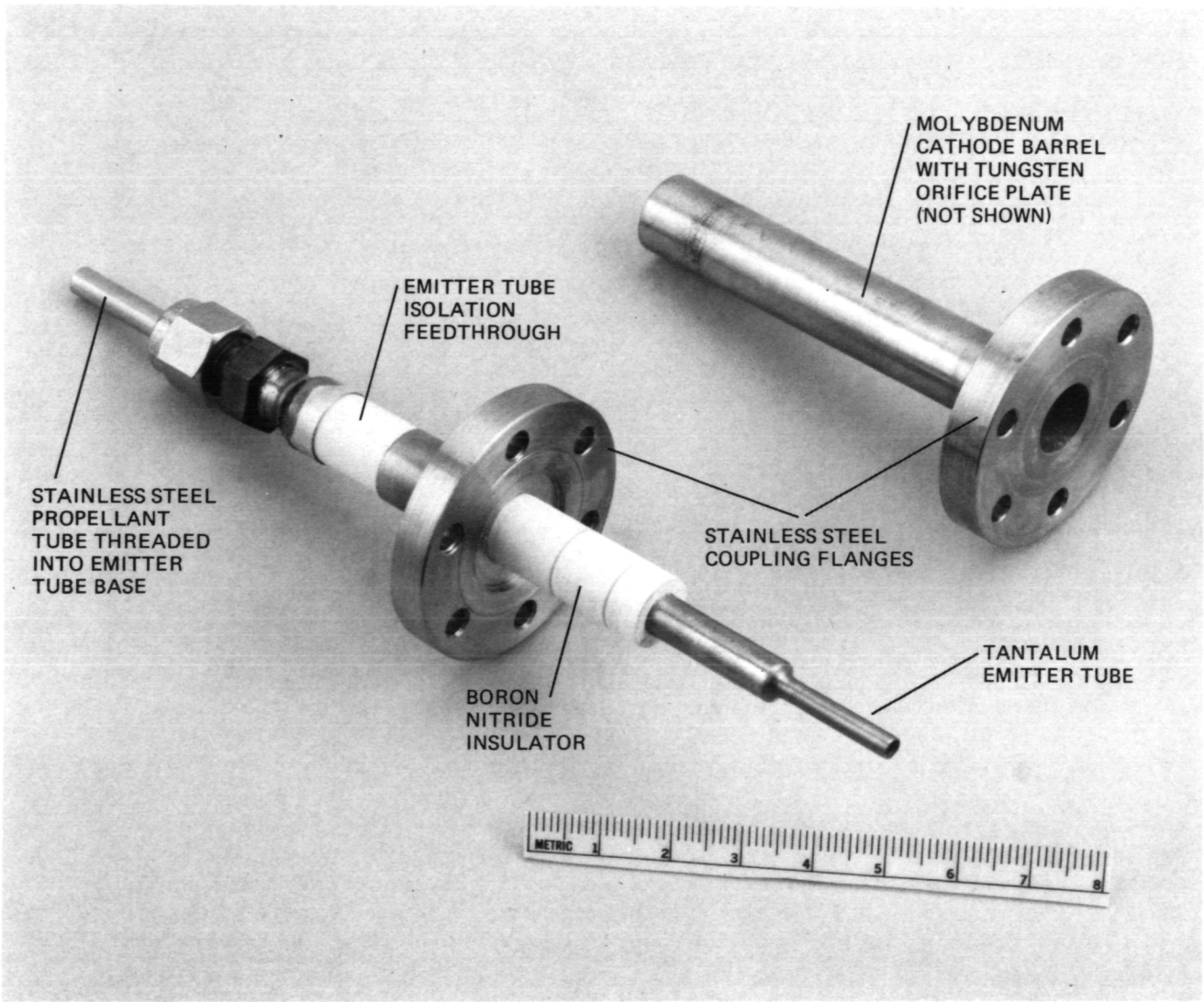

Fig. 5. FERM Hollow Cathode Major Components

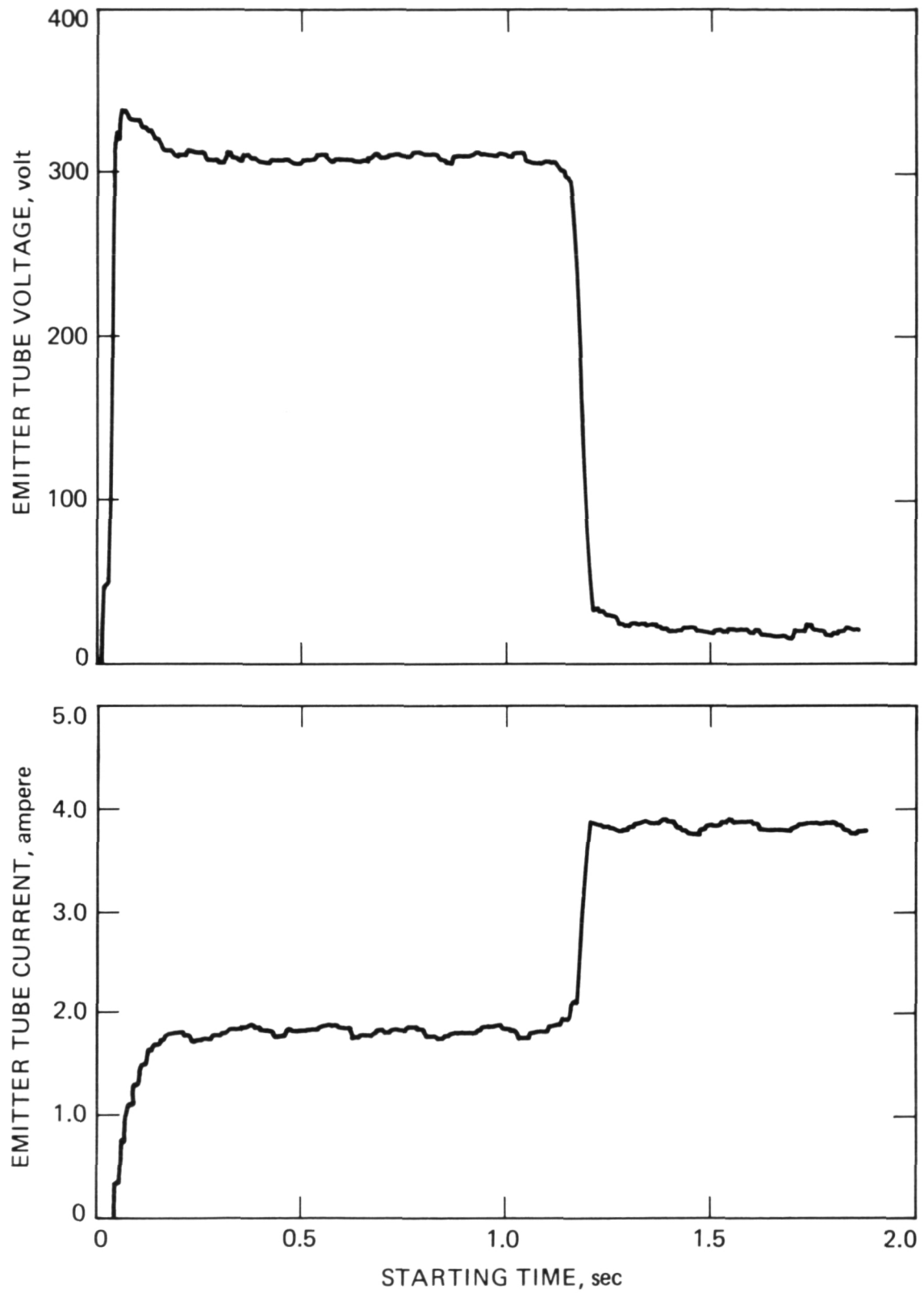

Fig. 6. FERM Cathode Starting Characteristics

upon the heat capacity of the last few millimeters of the emitter tube. Once started, the minimum power required to maintain a stable arc is approximately 100 watts.

2.2.2 Electron Emission Characteristics

Electron emission currents up to 35 amperes have been extracted from the tantalum emitter tube, through the 1.0 mm diameter tungsten orifice, during TBI engine operation. Arc attachment evidence on the emitter tube end shows that only the last 4-5 mm are involved in the electron emission process. Assuming emission from the inner and outer surfaces of this tube, the electron current density is approximately 50 amp/cm^2 at 35 amperes. Normally, such large sustained current densities, with metallic emitting surfaces, would result in melting and rapid evaporation because of the very high surface temperature required. However, within the environment of the dense hollow cathode plasma, the strong plasma sheath electric fields adjacent to the inner tube surfaces effectively lower the work function of the tube metal. This process has been suggested by Seigfried[4] as important in conventional oxide thruster hollow cathodes and is even more important in the FERM cathode. The effect of even slight reductions in work function, on electron current density, is substantial. Figure 7 plots current density for tantalum, as predicted by the Richardson-Dushman equation, against tube surface temperature with the surface work function as a parameter. In addition to the work function reduction, significant tube cooling occurs because of the energy removal associated with the electron emission process. Both of these factors are important for successful FERM cathode operation at high electron emission levels.

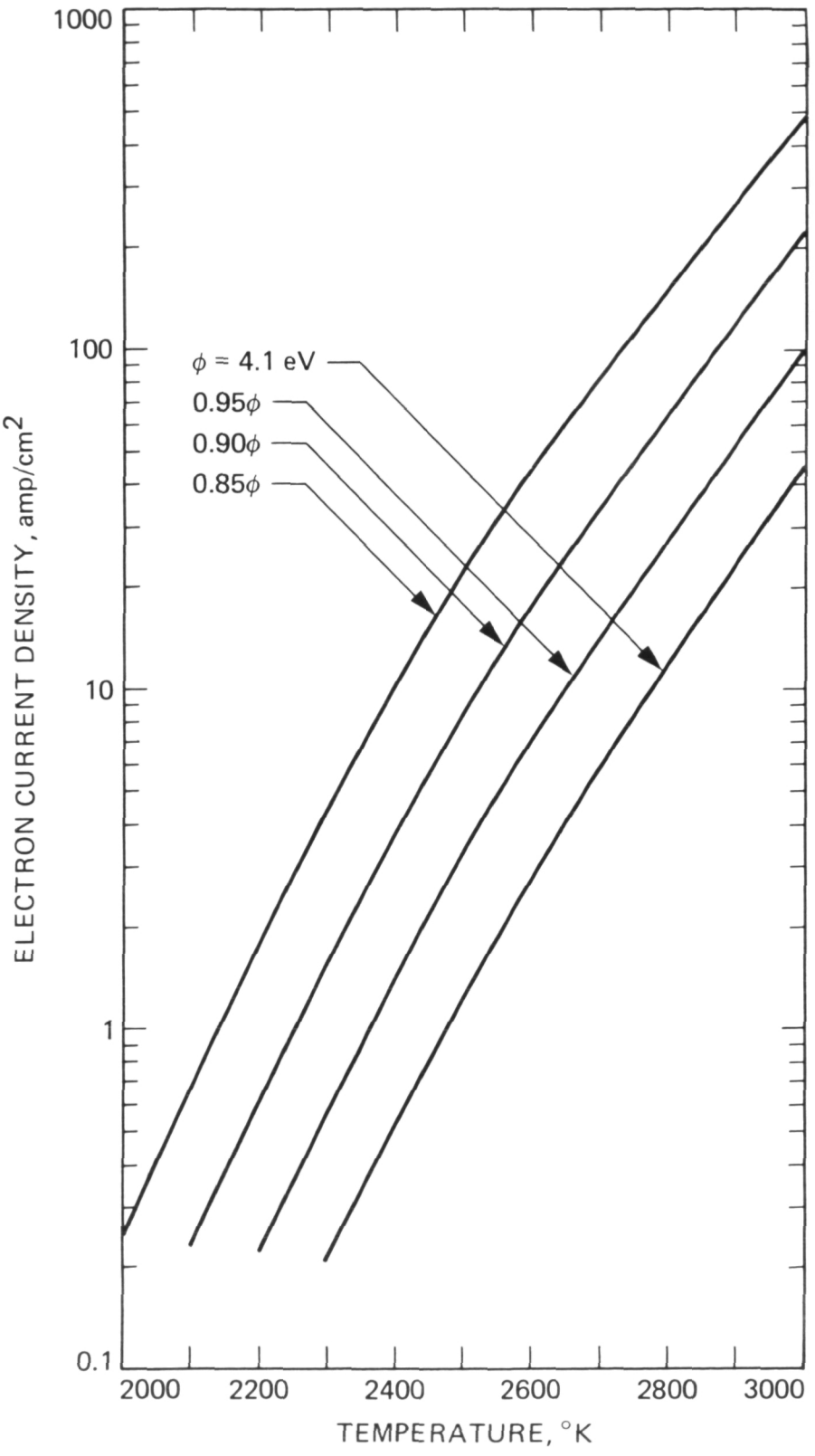

Fig. 7. Tantalum Thermionic Electron Emission Characteristics

2.2.3 Starting Pressure Requirements

An important parameter in successfully starting the FERM cathode is ensuring that the internal stagnation gas pressure is high enough to be in the correct region of the Paschen break down curve. For the FERM cathode barrel and emitter tube geometry, low Paschen break down voltages are realized, for most gasses, with a pressure distance product of about 1.0 Torr-cm.[5] Assuming a typical emitter tube-to-orifice plate (or cathode barrel) distance of 0.5 cm, the required starting FERM cathode gas pressure is approximately 2.0 Torr. Calculations were performed to determine the FERM cathode stagnation gas pressure in terms of the orifice geometry and gas specie. However, the results were unsatisfactory because of difficulty in accurately accounting for the effects of machining irregularities in forming the orifice. An accurate determination of stagnation gas pressure was achieved by conducting a series of experiments measuring this parameter for different orifice diameters, plate thicknesses and gasses. A Kinney Measuvac Type TDI MK III diaphragm mercury McCleod gauge was plumbed directly into the cathode barrel to take these measurements. Figures 8a, b, and c plot the recorded stagnation pressure against flow rate, with a range of gasses, for each orifice plate tested.

2.3 DLC DISCHARGE CHAMBER

Substantial reductions in ion thruster discharge loss levels have recently been realized by using high magnetic field strength plasma containment schemes.[6,7] The Divergent Line Cusp discharge chamber, shown in Fig. 9, borrows heavily from this prior work but departs from traditional ion thruster designs by its pyramid shape, which obviates the need for a back plate. In addition, the line cusp samarium cobalt magnets are located

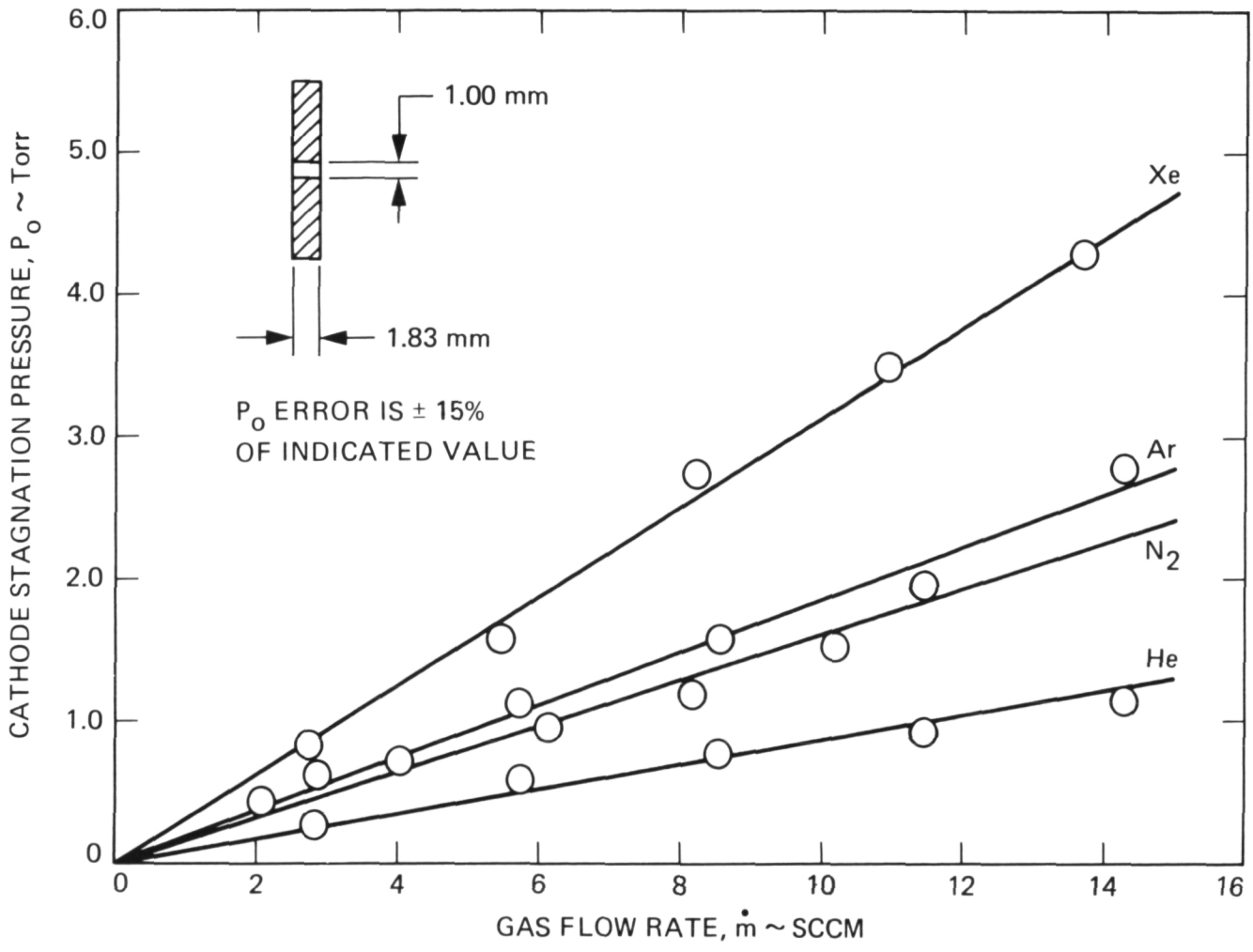

Fig. 8a. Stagnation Pressure Measurements: Thick Orifice Plate, Small Orifice

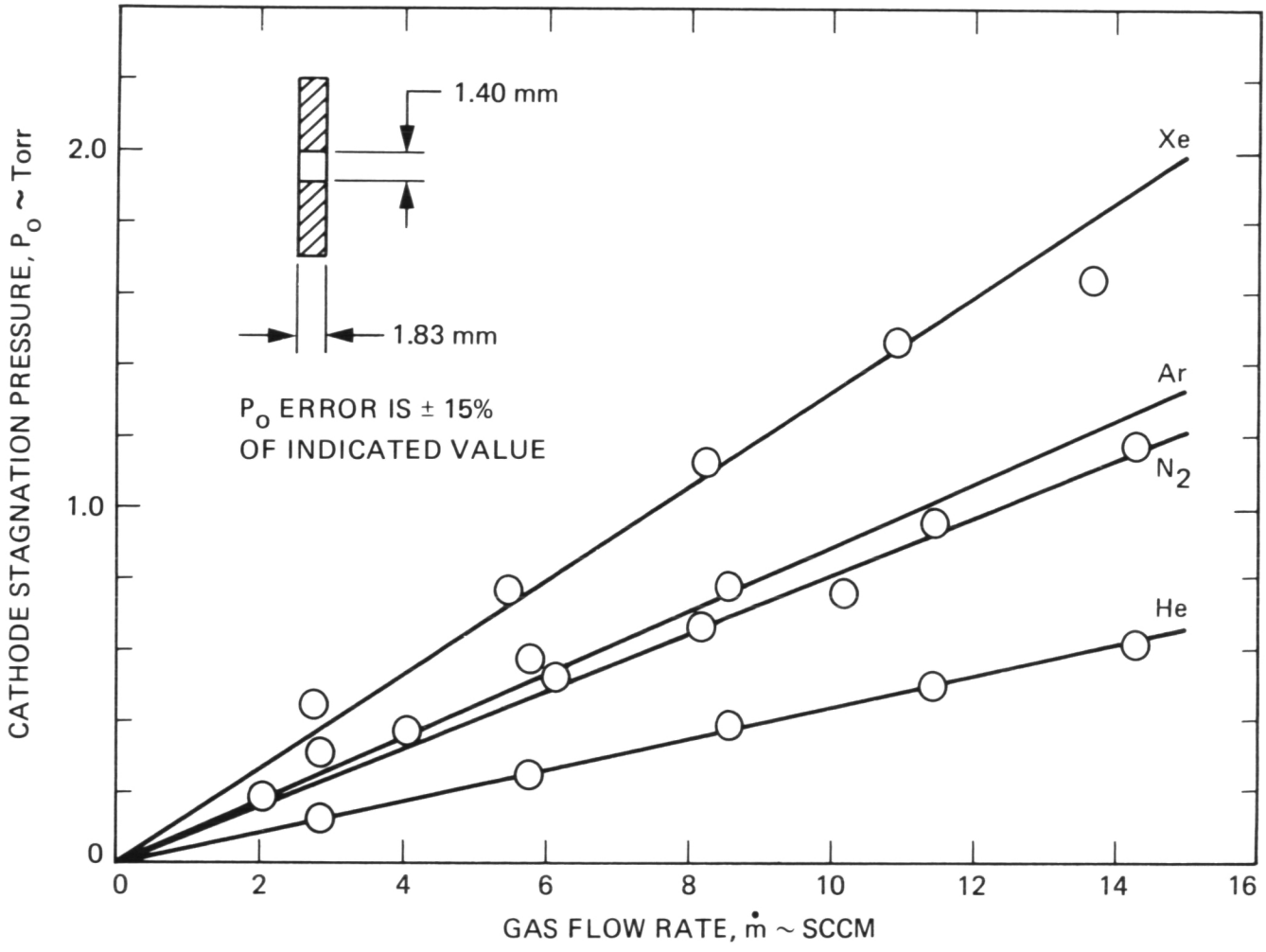

Fig. 8b. Stagnation Pressure Measurements: Thick Orifice Plate, Large Orifice

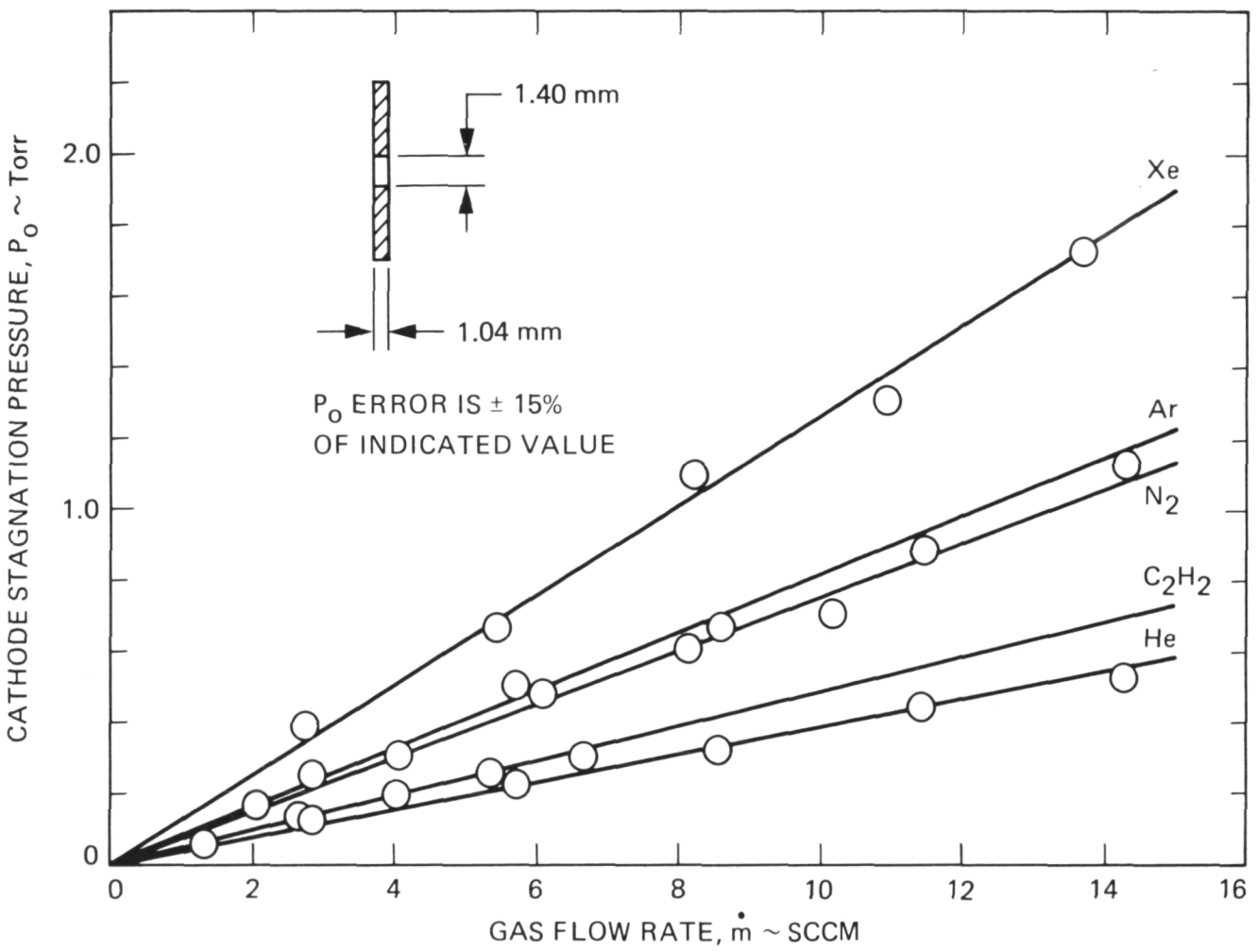

Fig. 8c. Stagnation Pressure Measurements: Thin Orifice Plate, Large Orifice

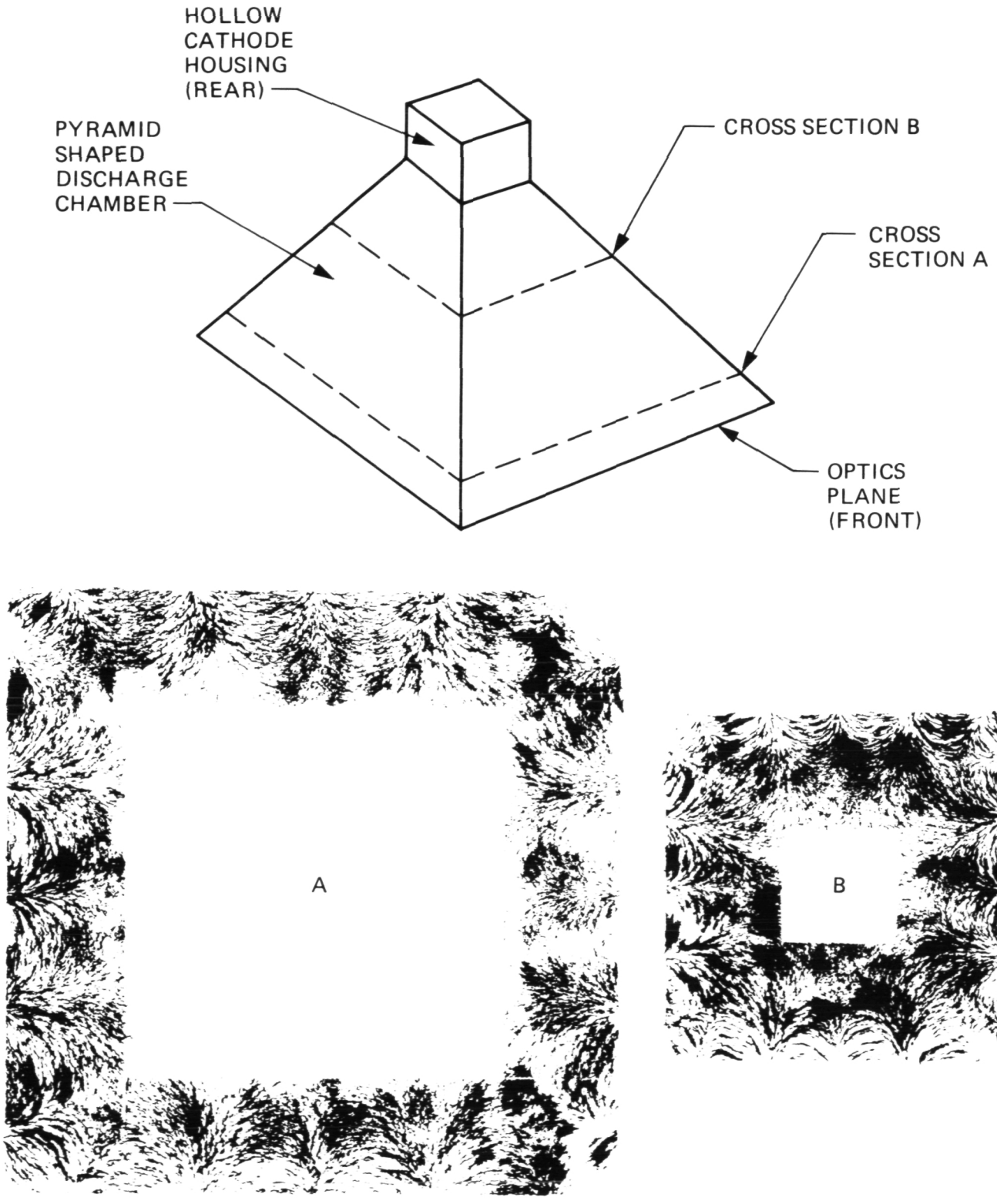

Fig. 9. DLC Discharge Chamber and Magnetic Field Geometry

external to the discharge chamber. The magnetic field distribution along the chamber inner surface is such that linear cusps are formed between the cathode location and the chamber exit plane. The magnetic field intensity, at the cusps, is intense at the cathode plane and decreases toward the exit plane. By tapering the line cusps in this manner it was also felt that easy cathode to anode coupling (the entire DLC chamber is at anode potential in Fig. 9) would be assured because of the large magnetic impedance variation to electron flow.

SECTION 3

TEST BED ION ENGINE

The DE-AC accelerator system, FERM hollow cathode and DLC discharge chamber consitute the Test Bed Ion Engine. This section describes the unique engine design and construction methods which resulted in a minimum of structural components yet retained the versatility of being able to change critical cathode and accelerator system parameters throughout the test program. Results of extensive performance tests are presented which provide a basis for determining the maximum thrust density of this technology.

3.1 SPECIFICATIONS AND CONSTRUCTION DETAILS

3.1.1 Cooling and Mechanical Design

One of the most important considerations in the mechanical design of the TBI engine was to provide adequate cooling. This requirement was motivated by a need to operate the engine at high discharge power levels (>1.0 kW) while keeping the samarium cobalt magnets well below their demagnetizing threshold (~250^{o}C). Further compounding the cooling problem was an inability to radiate any substantial heat flux through the front of the engine. This was so because most of the discharge chamber face was to be masked off so that only small, easily modified, DE-AC accelerator system modules could be tested. Finally, manufacturing cost considerations dictated aluminum as the preferred TBI engine fabrication material. All of these constraints ultimately lead to water cooling of the entire TBI engine as the most satisfactory way to guarantee low engine operating temperatures. Since the engine was a technology test bed, water cooling was an acceptable solution.

Figure 10 shows the complete TBI engine mounted on the vacuum facility bulkhead. Although only a small DE-AC accelerator system is shown, the area available for useful ion extraction, with this engine, is a square approximately 25 cm x 25 cm. Detailed drawings of the TBI engine are shown in Fig. 11. The samarium-cobalt magnets were cut and ground to a length of 5.72 cm a height of 1.270 cm and a width of 0.508 cm. These magnets were magnetized parallel to their 1.270 cm dimension. Cooling water passages were milled into the discharge chamber side plates and routed to pass by each magnet location slot. An aluminum thickness of 0.076 cm separated each magnet pole face from the discharge chamber plasma. With this spacing the cusp magnetic field flux density was 2500 gauss. The DLC discharge chamber was assembled from four side plates identical to that shown in Fig. 12. These plates, the optics mounting flange and the water cooled cathode mounting block, were inert gas welded into one integral gas tight structure. The sheathing covering the side plates to seal off the milled water passages and the water inlet and outlet ports for each plate were salt dip brazed in one simultaneous operation.

3.1.2 Cathode and Langmuir Probe Location

Since the magnets were external to the discharge chamber the interior of the TBI engine contained only the FERM cathode as shown in Fig. 13. For diagnostic purposes, a Langmuir probe was also placed in the chamber. This probe could be moved, axially, from a position slightly to the rear of the cathode orifice plate to just upstream of the DE-AC accelerator system. Arc attachment lines on the DLC discharge chamber, in Fig. 13, clearly define the magnetic cusp placement. Also, as can be seen from this figure, no cathode keeper or external tickler electrode is required when using

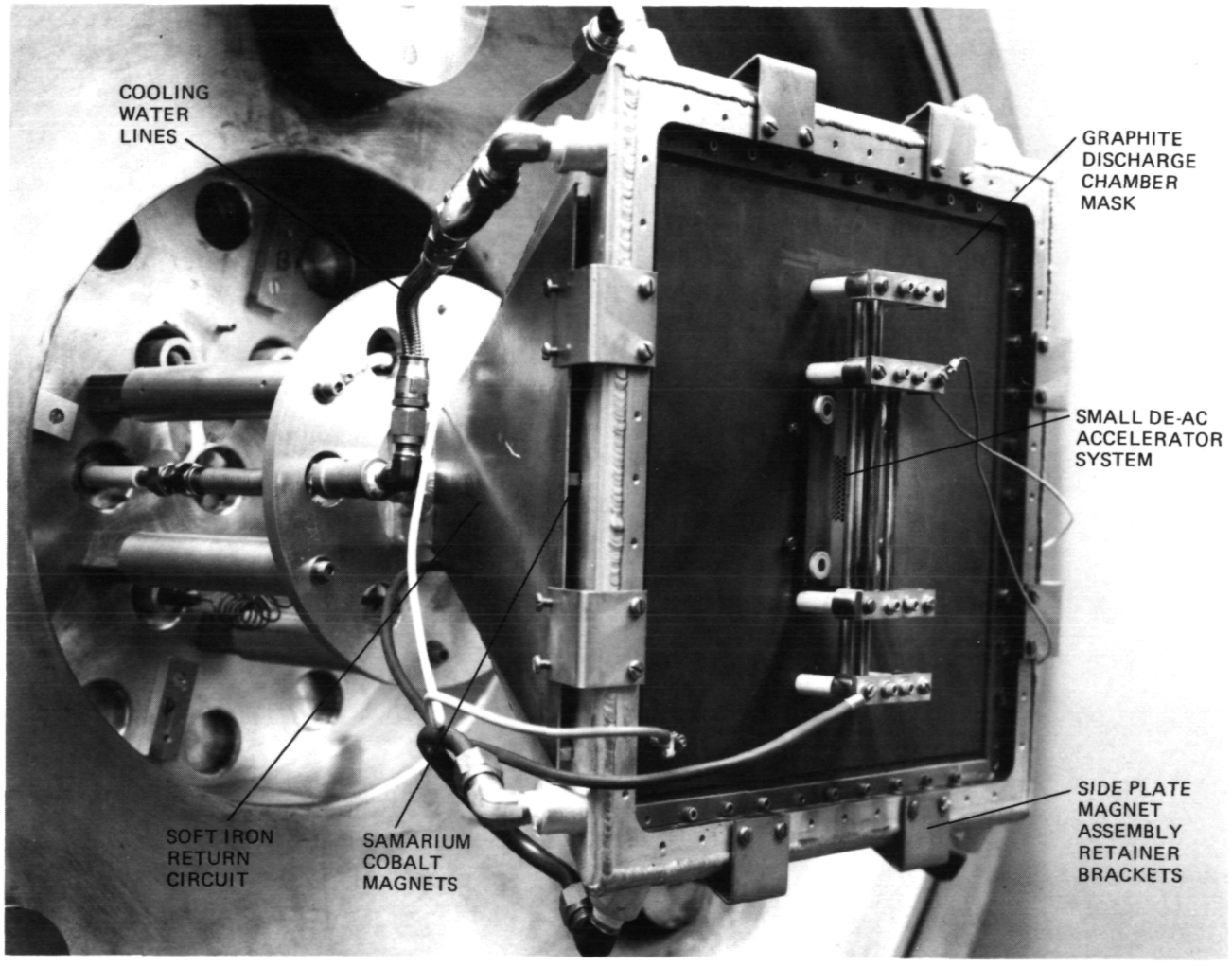

Fig. 10. TBI Engine Mounted on the Vacuum Tank Bulkhead

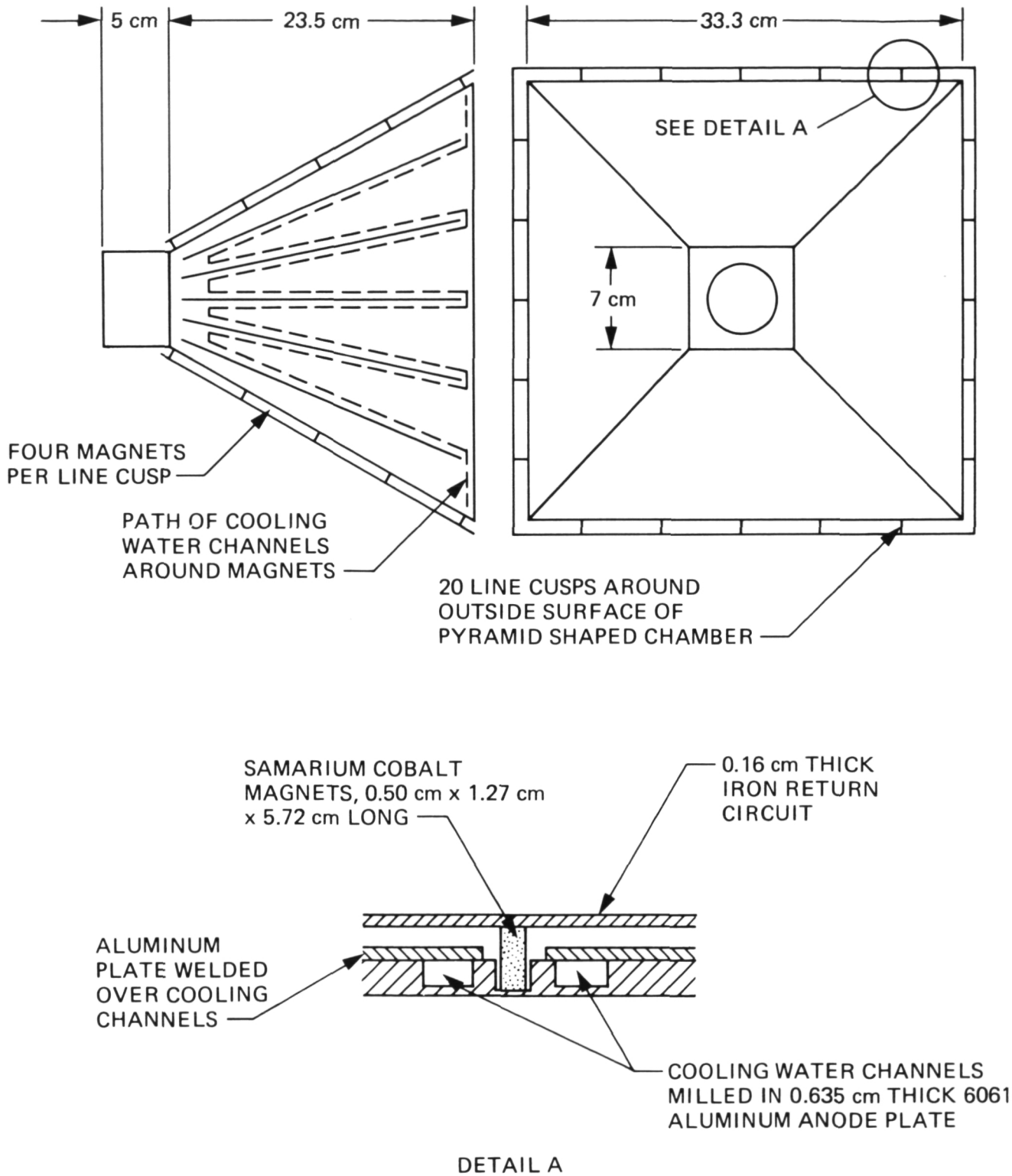

Fig. 11. Major TBI Engine Design Details

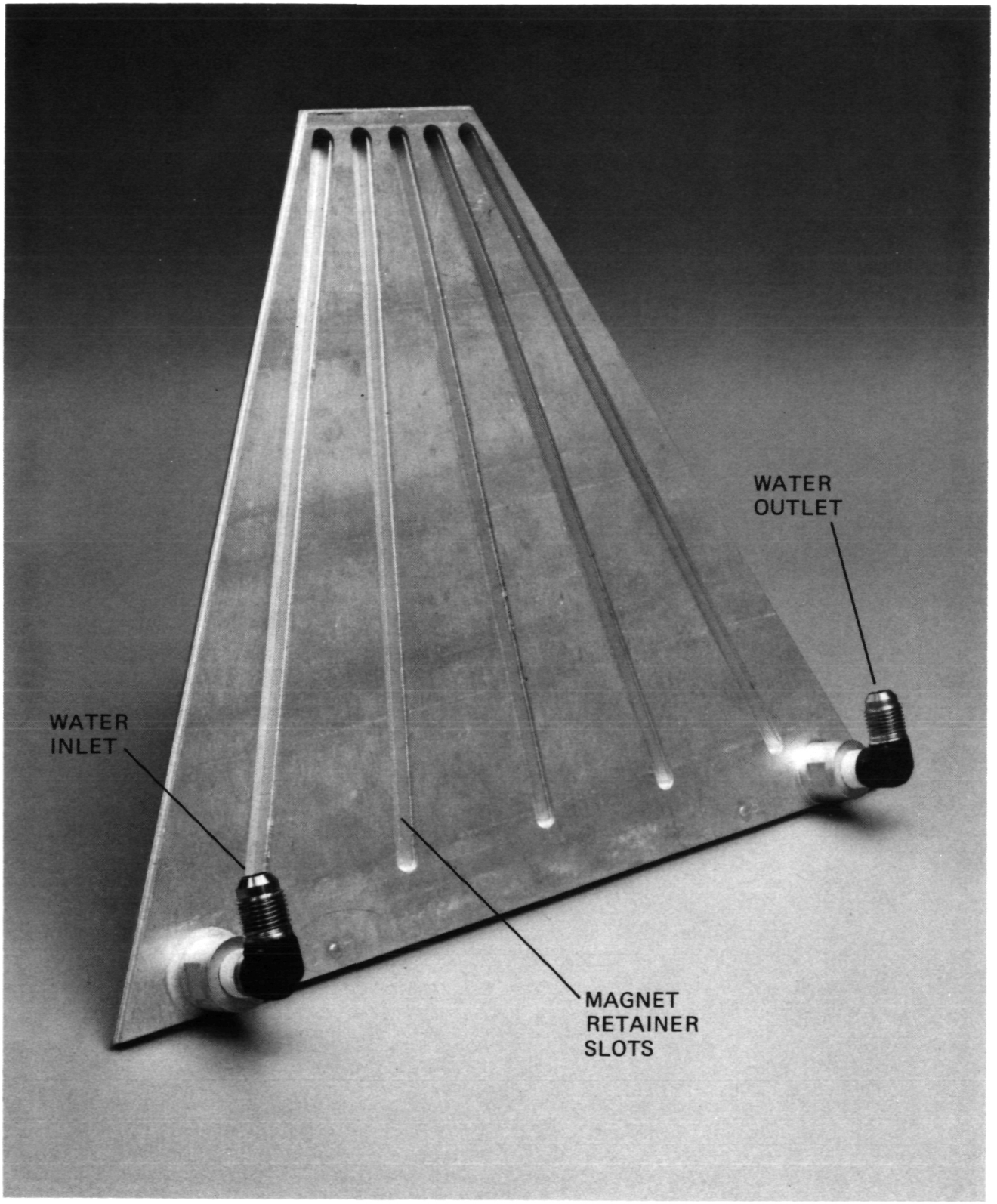

Fig. 12. DLC Discharge Chamber Side Plate Prior to Final Assembly

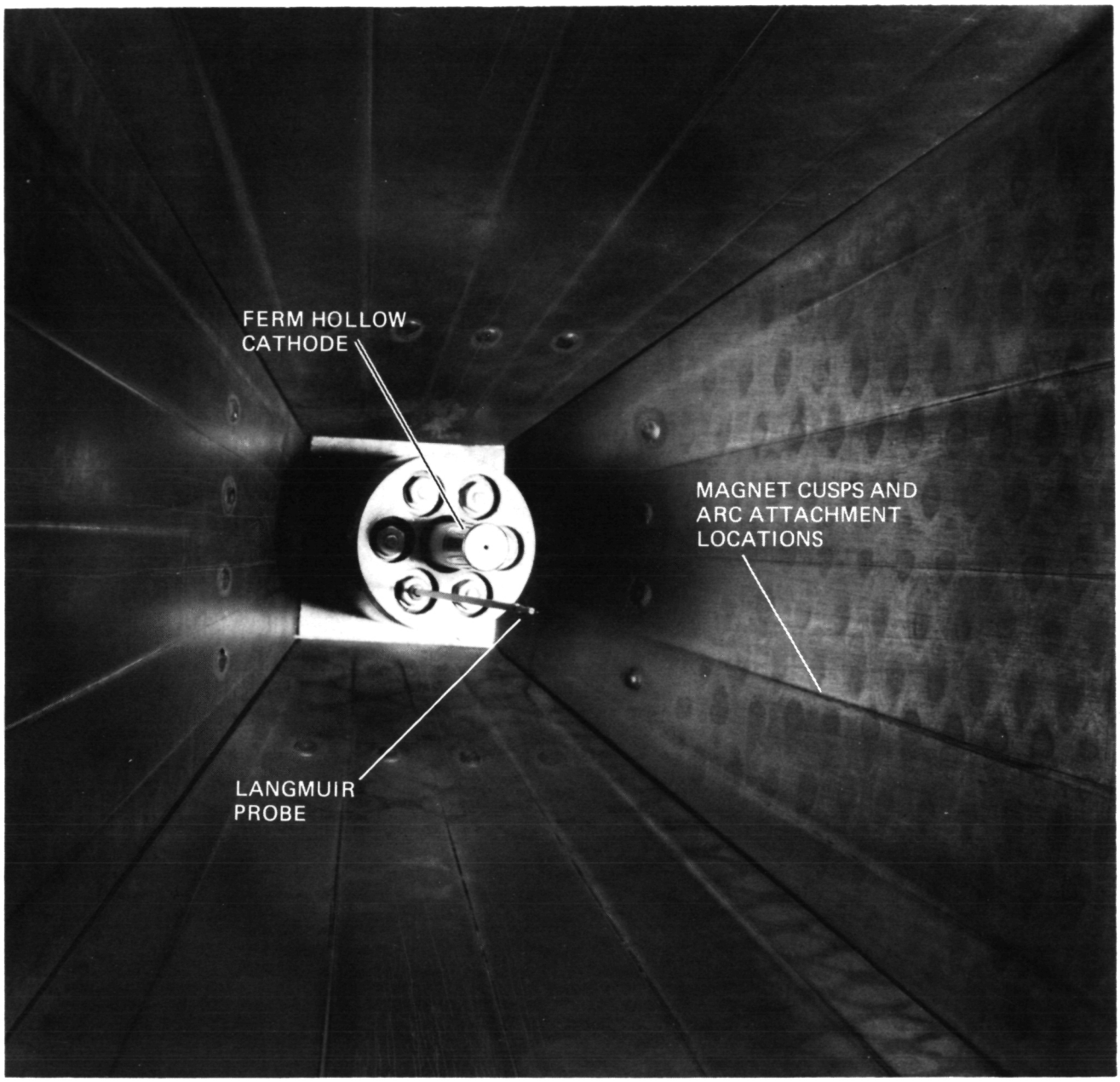

Fig. 13. Interior of TBI Engine

the FERM hollow cathode. Figure 14 shows the cathode removed from the engine and inside a stainless steel slip tube which permitted the entire assembly to be positioned at different axial locations within the discharge chamber. The FERM cathode is shown in Fig. 15 removed from its slip tube but still bolted to the boron nitride block which isolated the cathode body from engine anode potential.

3.2 SUPPORT FACILITY

3.2.1 Vacuum Tank and Power Supplies

All TBI engine tests were done in a 0.9 m diameter x 2.1 m long non-magnetic stainless steel vacuum tank pumped by two 0.25 m diameter silicon oil diffusion pumps. The cryo traps of these pumps were filled with alcohol and cooled to $-50^{o}C$ by refrigerated immersion probes. Typical no load tank pressure was $1.0\text{-}2.0 \times 10^{-6}$ Torr with an $8.0\text{-}10.0 \times 10^{-5}$ Torr pressure range during TBI engine operation. Figure 16 shows the vacuum tank, control console and accompanying engine power supply rack and flow control system.

Four power supplies were used at different times to start and operate the TBI engine. The screen and accelerator supplies were Hippotronic unregulated 0-1 kV and 0-20 kV, 1 kW units respectively. A 0-500V, 5A low duty cycle unregulated supply was used to start the FERM cathode and was turned off when the anode discharge was established. The anode power supply was a laboratory assembled constant current unit with an 80 volt compliance voltage and a 0-35A current range. No neutralizer was used with the TBI engine since refractory filament neutralizer tests, made at the start of the test program, showed no change in ion beam quality or engine performance when the beam was self neutralized by secondary electron emission from the vacuum tank walls.

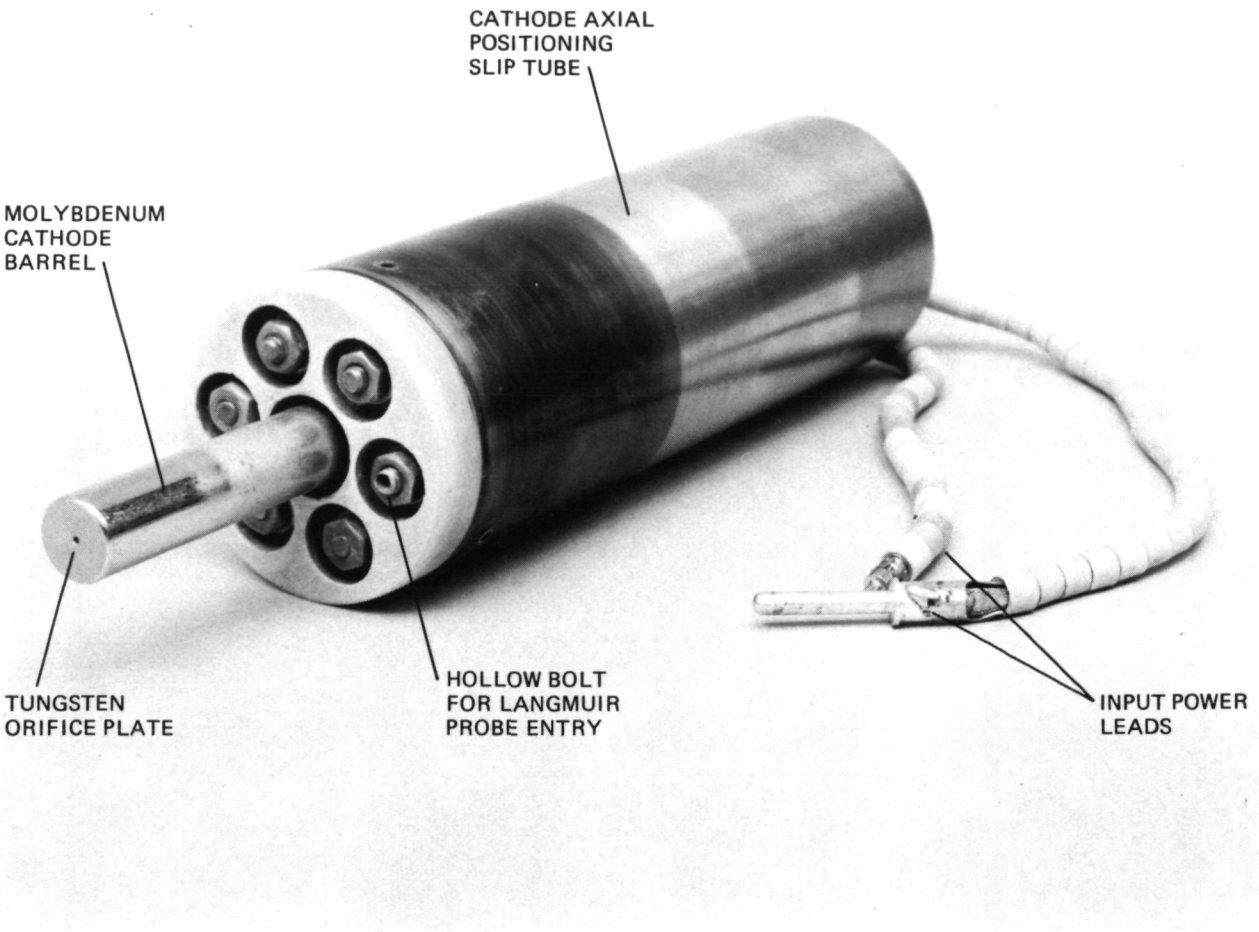

Fig. 14. FERM Cathode in Slip Tube

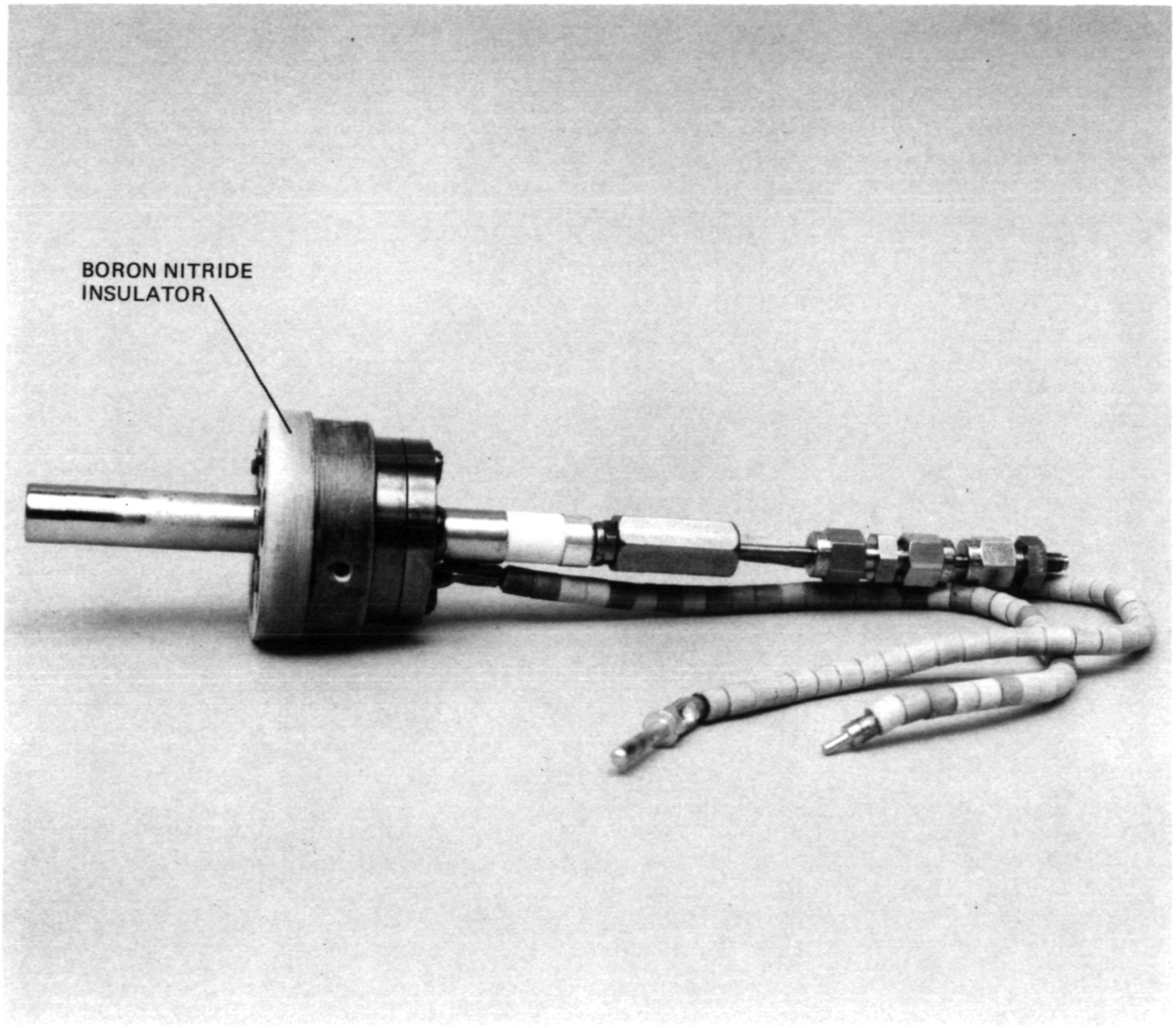

Fig. 15. Method of FERM Cathode Isolation

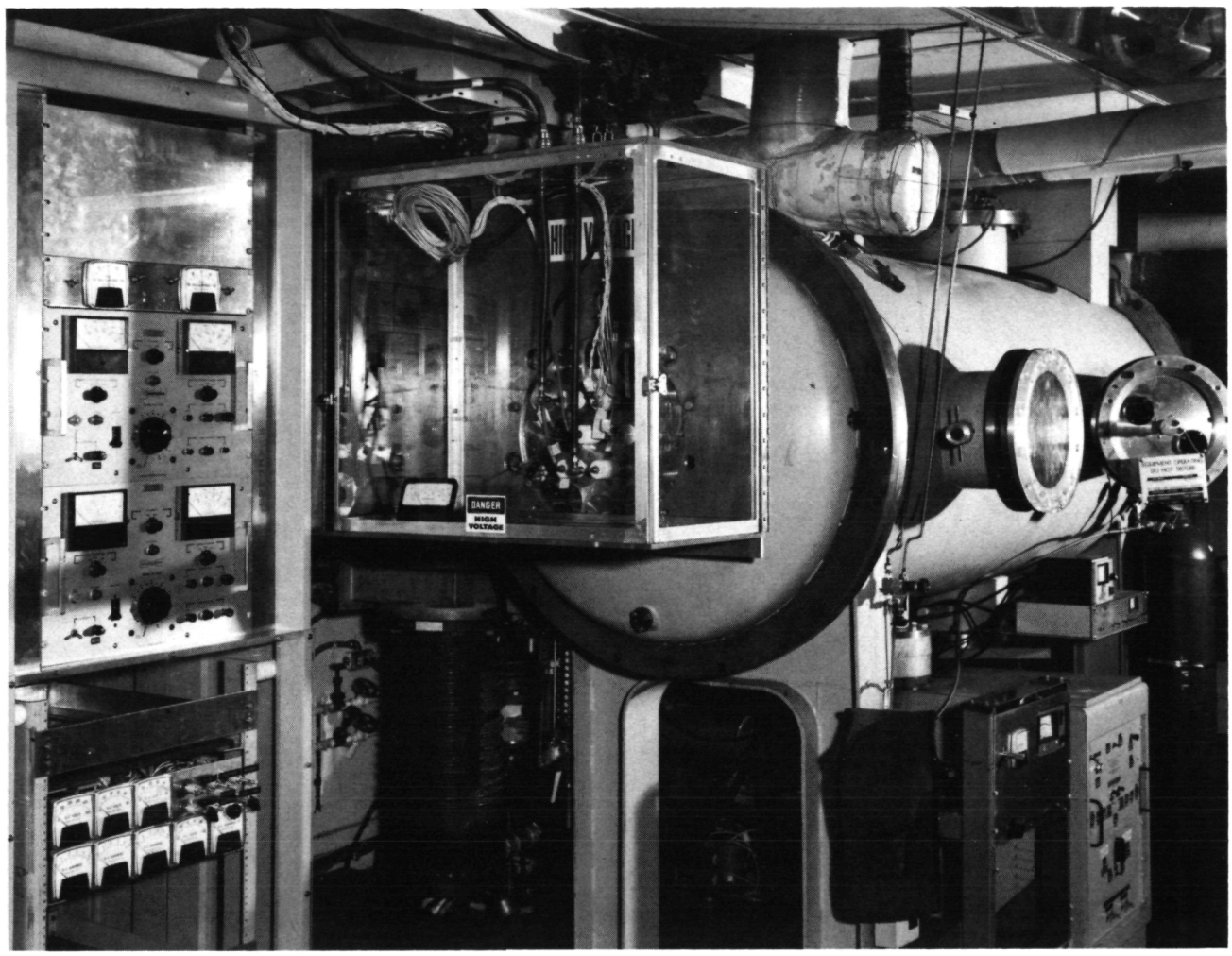

Fig. 16. TBI Engine Test Facility

3.2.2 Beam Probe System

An x-y probe carriage for beam diagnostics was installed in the vacuum facility as shown in Fig. 17. The probe carriage base consisted of a square aluminum frame with two parallel aluminum tracks rigidly attached to it on opposite corners. A motor driven lead screw was attached across the diagonal of the probe carriage base, parallel to the two tracks. Movement parallel to this lead screw was defined as motion in the y direction. An aluminum track was attached to the pillow block on the base lead screw. This track was orthogonal to the base lead screw and the two tracks on the base. Bearings attached to this track allowed it to be guided along the parallel tracks on the base, by the base lead screw. In addition, a lead screw and motor assembly, similar to those on the base, were attached to this track. A probe platform was attached to the pillow block on this lead screw and bearings attached to the platform guided it along the track. Movement parallel to this lead screw was defined as motion in the x direction. The whole apparatus was hung in the vacuum facility such that the lead screw attached to the base was vertical. Gear assemblies attached to each lead screw drove ten turn potentiometers which indicated the probe position as a function of output voltage. There was 56.8 cm of travel in the x direction and 30.0 cm of travel in the y direction.

A single Faraday probe was used for all beam current density measurements. This probe can be seen within the center of the large disc evident in Fig. 17. Probe fabrication details are shown in Fig. 18. The probe ion collection surface and surrounding guard ring were biased at +18.0 volts to repel low energy, charge exchange, ions and prevent the loss of secondary electrons from the probe surface. An 81% open area tungsten screen biased at -18 volts, with respect to facility ground, prevented beam plasma

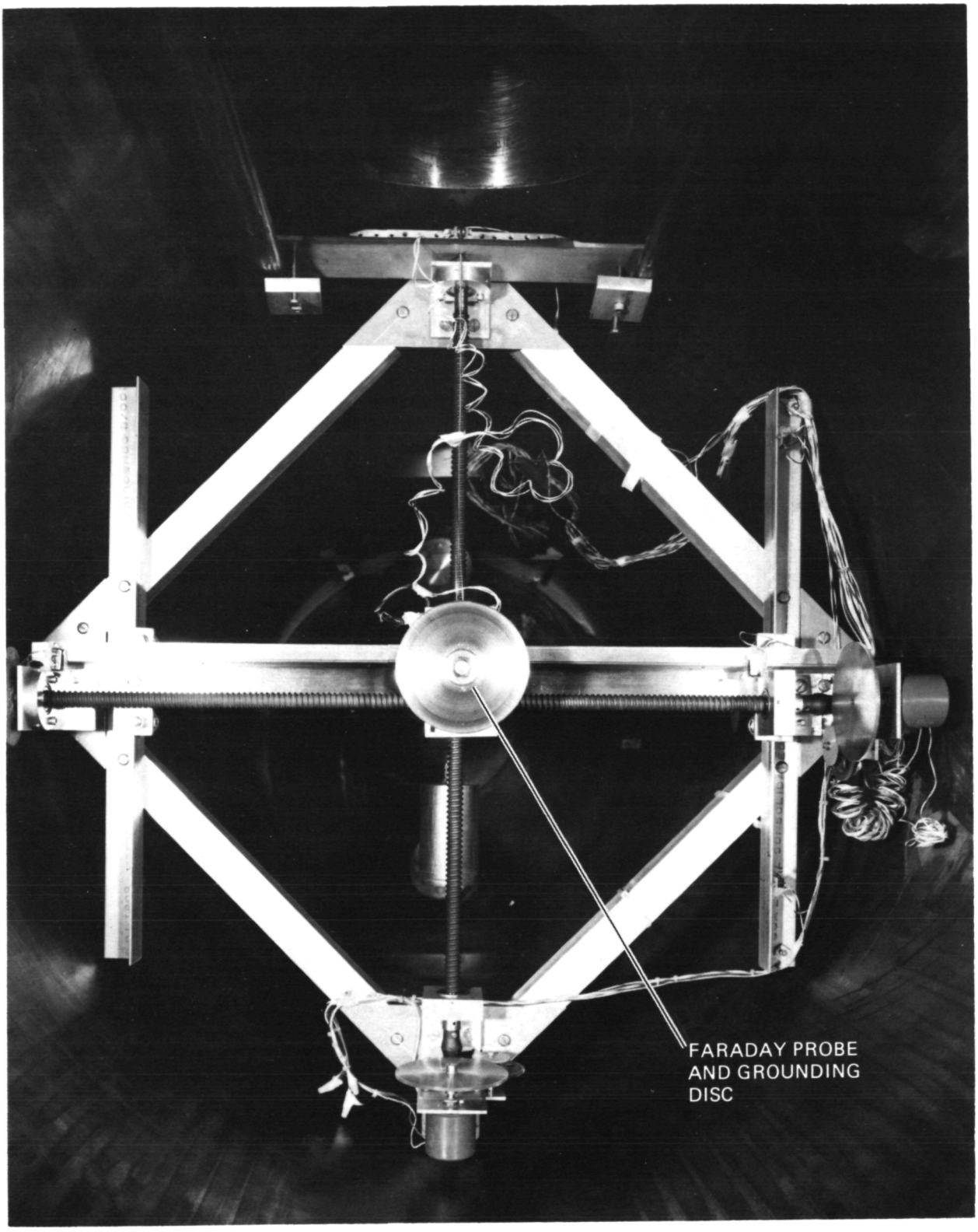

Fig. 17. X-Y Beam Probe Carriage

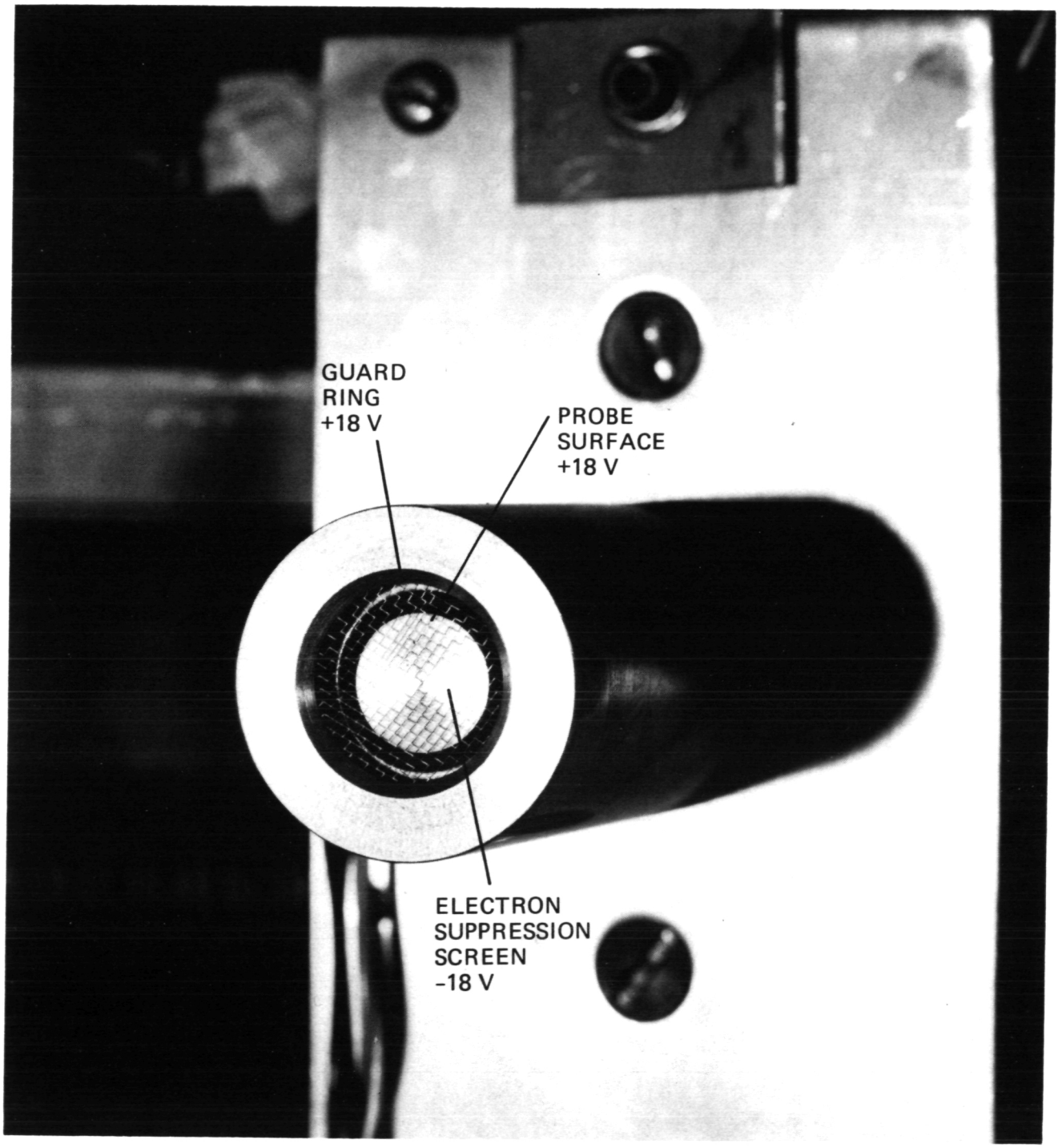

Fig. 18. Faraday Beam Ion Probe

electrons from reaching the probe. The large disc attached to this negatively biased screen and probe body ensured uniform beam neutralization within the immediate vicinity of the probe.

3.3 DISCHARGE CHAMBER PERFORMANCE

Early in the test program it became apparent that the plasma property characteristics of the FERM cathode and DLC discharge chamber combination were unusual. To better understand the observed behavior, a considerable effort was expended on documenting those plasma property values most useful in describing the plasma generation and containment processes.

3.3.1 V-I Characteristics

Figure 19 shows typical arc discharge current and voltage characteristics for the TBI engine. For these data, all of the indicated argon gas flow was passing through the FERM hollow cathode, which was operated in the self heating mode. Also, as mentioned earlier, the downstream end of the TBI engine was almost completely masked over, for this test program, so that low gas flow rates corresponded to high neutral gas pressures within the engine.

The V-I characteristics in Fig. 19 illustrate a trend of low discharge voltages at high discharge currents as the discharge chamber neutral number density increases (i.e. increasing flow rate). Of equal interest is the low potential the floating FERM cathode body assumes relative to the inner electron emitting tube, V_C. Such low values of V_C should cause little backstreaming ion sputter erosion on the electron emitting tube. The V-I characteristics of the TBI engine discharge plasma in Fig. 19, while very

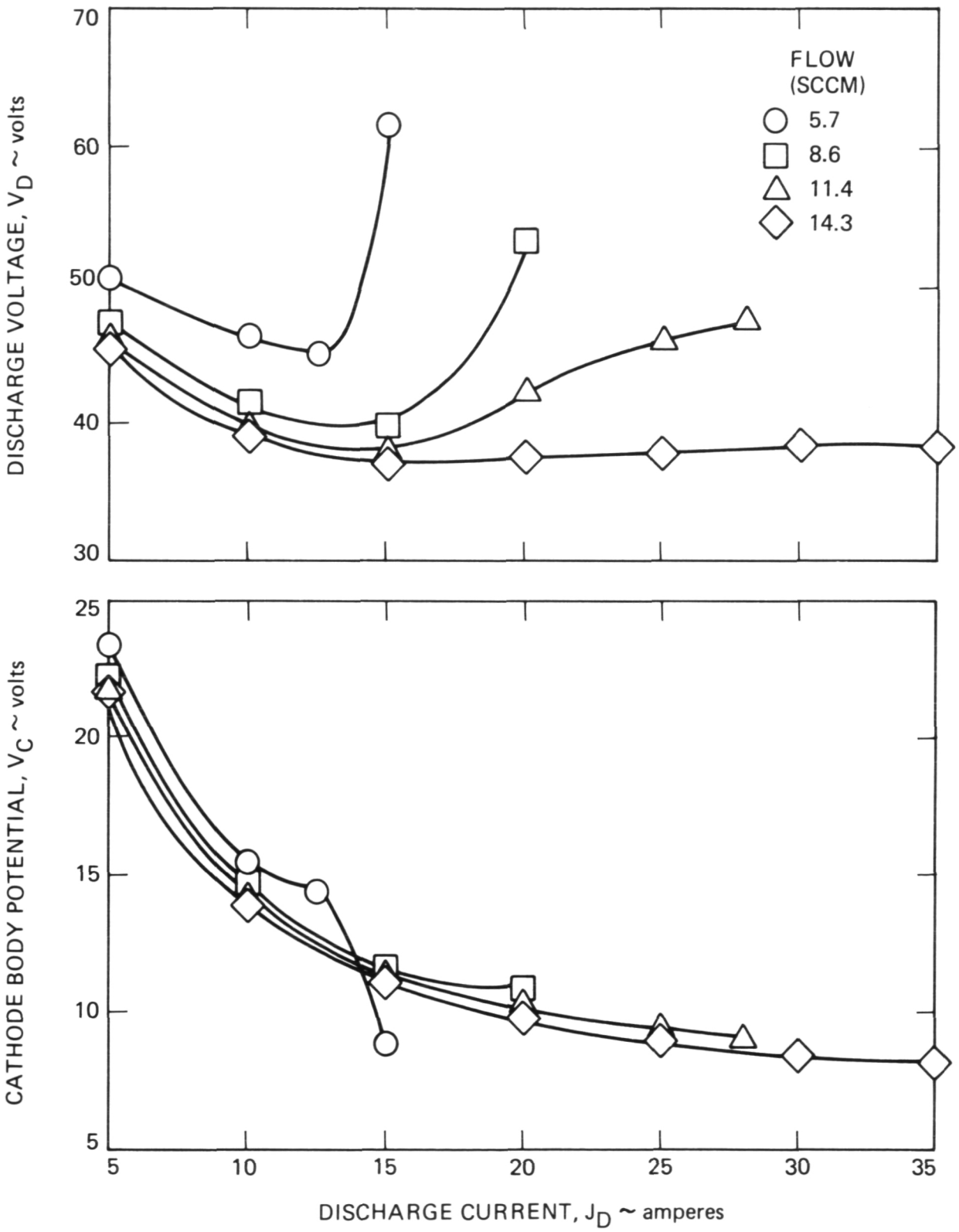

Fig. 19. TBI Engine Arc Discharge V-I Characteristics

encouraging, do need verification with an unmasked discharge chamber before meaningful comparisons with other ion engine designs can be made.

No life tests of the FERM cathode or DLC discharge chamber were performed. Nevertheless, a few tens of hours total operating time were accumulated on these components and some comments can be made. Erosion of the FERM cathode orifice appears similar to that of present ion thruster oxide hollow cathode designs wherein the downstream hole edges quickly become rounded with little further scalloping taking place. Cathode operation at high discharge power levels (>1.0 kW) did cause local melting of the emitter tube end. This component was made of tantalum and the substitution of tungsten is expected to correct this problem. Although arc discoloration lines clearly defined the samarium-cobalt magnet locations around the DLC discharge chamber (Fig. 13), there was no evidence of erosion or degradation of any portion of this aluminum structure.

3.3.2 Langmuir Probe Results

Approximately one hundred Langmuir probe traces were taken, within the TBI engine discharge chamber, throughout the duration of the test program. Three different cylindrical Langmuir probes were used, with tungsten rod diameters of 1.02, 0.51 and 0.25 mm. All of the data presented in the next few pages were obtained with the 0.25 mm dia. probe although consistant results were obtained with the other probes. Power for the probe bias circuit was provided by an isolated supply made up of 125 alkaline D cells. This supply provided a probe sweep range of from -50V to +100V with respect to the cathode electron emitting tube.

Probe trace analysis generally followed a procedure outlined by Beattie[8] and was done in several parts. First, the coefficients of a linear

plus exponential equation were obtained by curve fitting to the data in the electron retarding region. The intersection of this retarding region and the probe trace linear electron saturation region was determined iteratively using the Newton-Raphson method. Finally, using the thin sheath cylindrical probe equations of Langmuir, the Maxwellian electron temperature, plasma potential, Maxwellian electron density, primary electron temperature and primary-to-Maxwellian electron density ratio were determined for each probe trace.

For all the probe traces analyzed no significant primary electron population was found, even with the movable probe positioned close to the cathode orifice. Clearly, a primary electron population must exist in the TBI engine but it appears to be less than 5%, of the Maxwellian electron population, in those regions probed. It was felt that the small primary electron populations detected were within the error range of this difficult to determine parameter and so are not presented in this report. For all TBI engine operating conditions tested the Maxwellian electron densities presented can be assumed to be equal to the entire plasma electron density.

Figures 20 through 23 show the variation in plasma potential, Maxwellian electron density and Maxwellian electron temperature with increasing discharge current as a function of flow rate for four different Langmuir probe axial positions. For these data the axial position x=0 corresponded to the location of the DE-AC accelerator system screen grid, while the front of the cathode orifice plate was located at an axial postion of x=10.9 cm. Data collection and analysis uncertainties indicated a plasma potential error range of ±1.0 volt, a Maxwellian electron density error range of ±20% of the value indicated and a Maxwellian electron temperature error range of ±1.0 eV.

Several things are immediately apparent with the TBI engine plasma property data in Figs. 20 through 23. The measured plasma potential was

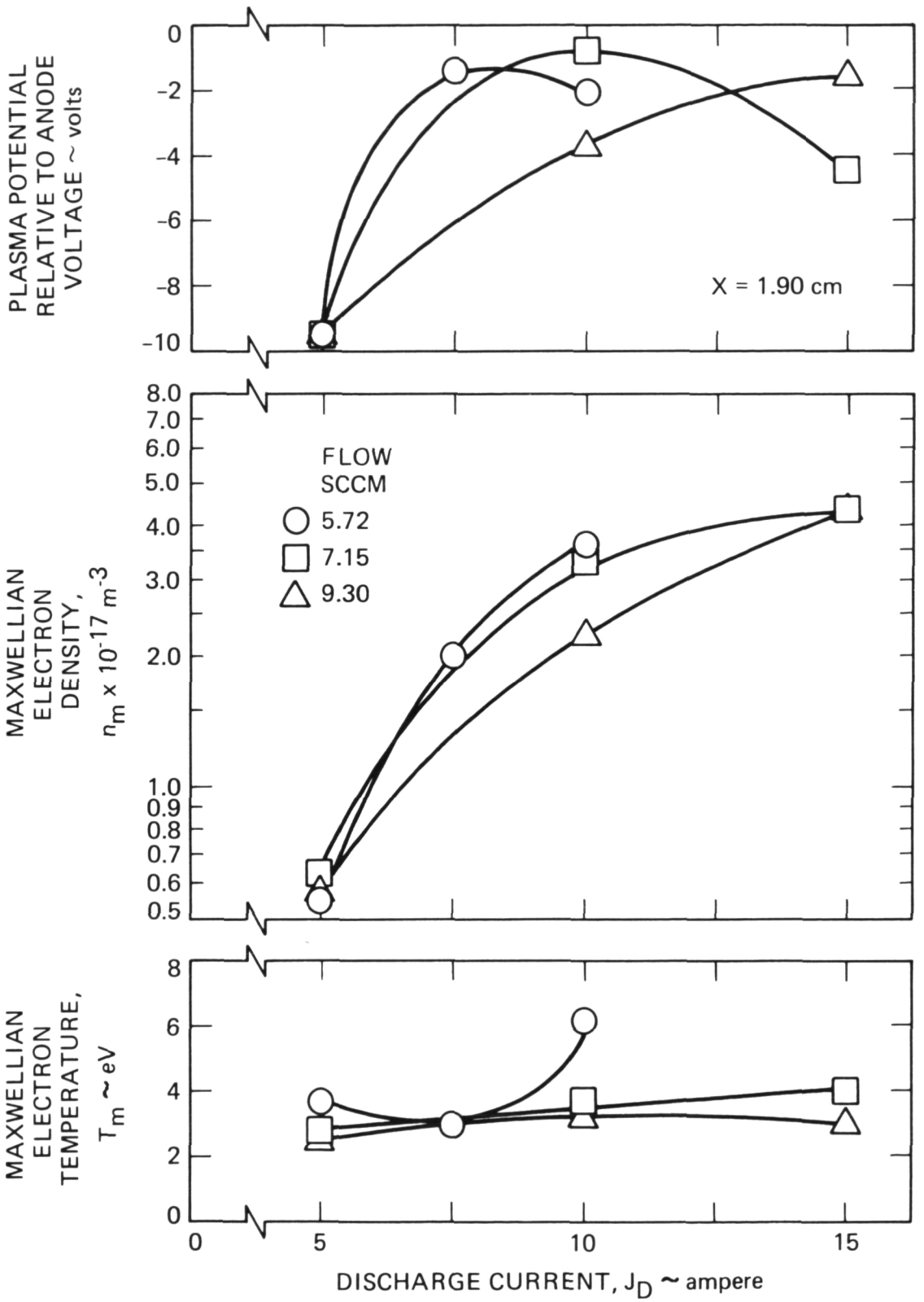

Fig. 20. TBI Engine Discharge Plasma Characteristics: x = 1.90 cm

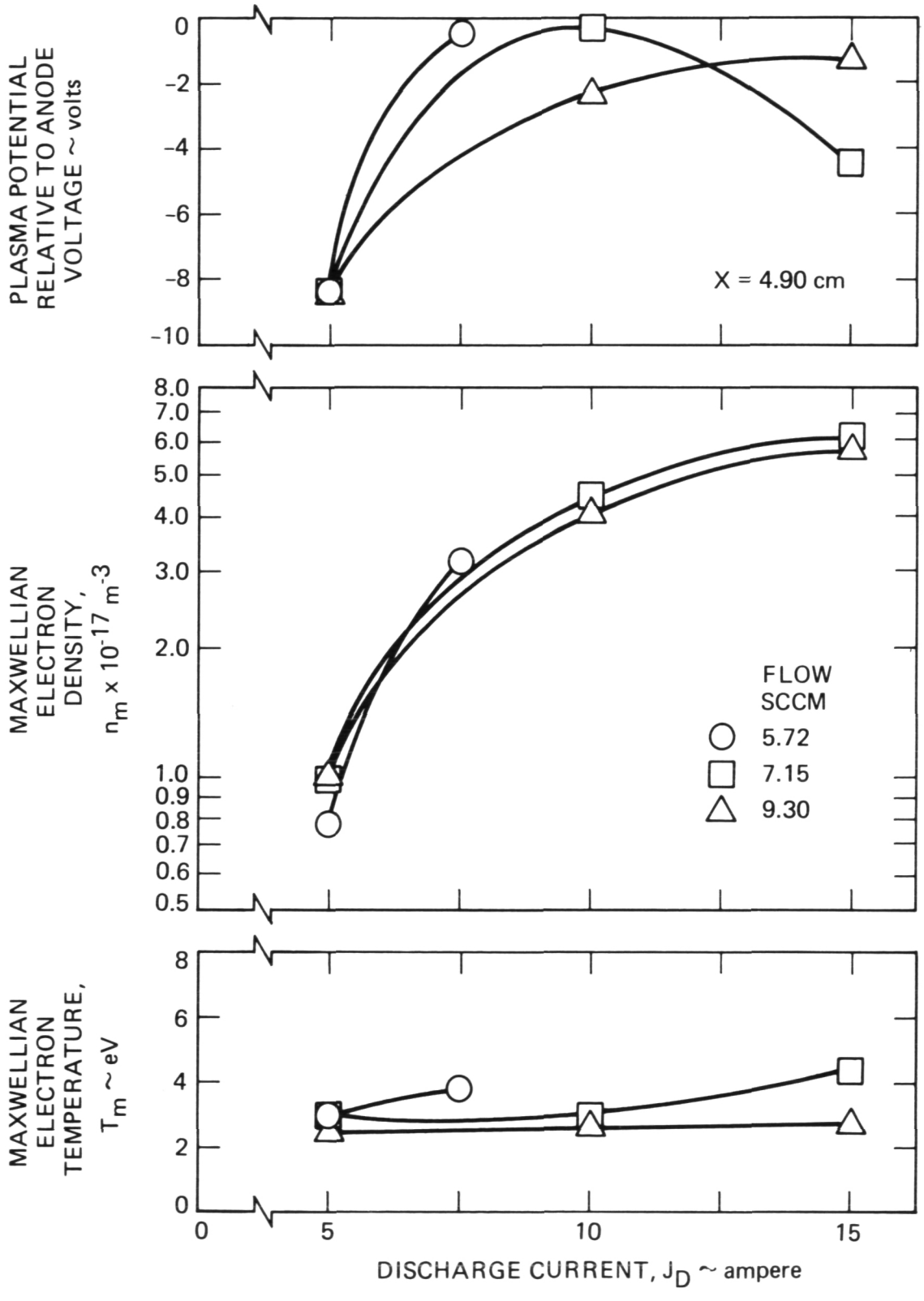

Fig. 21. TBI Engine Discharge Plasma Characteristics: x = 4.90 cm

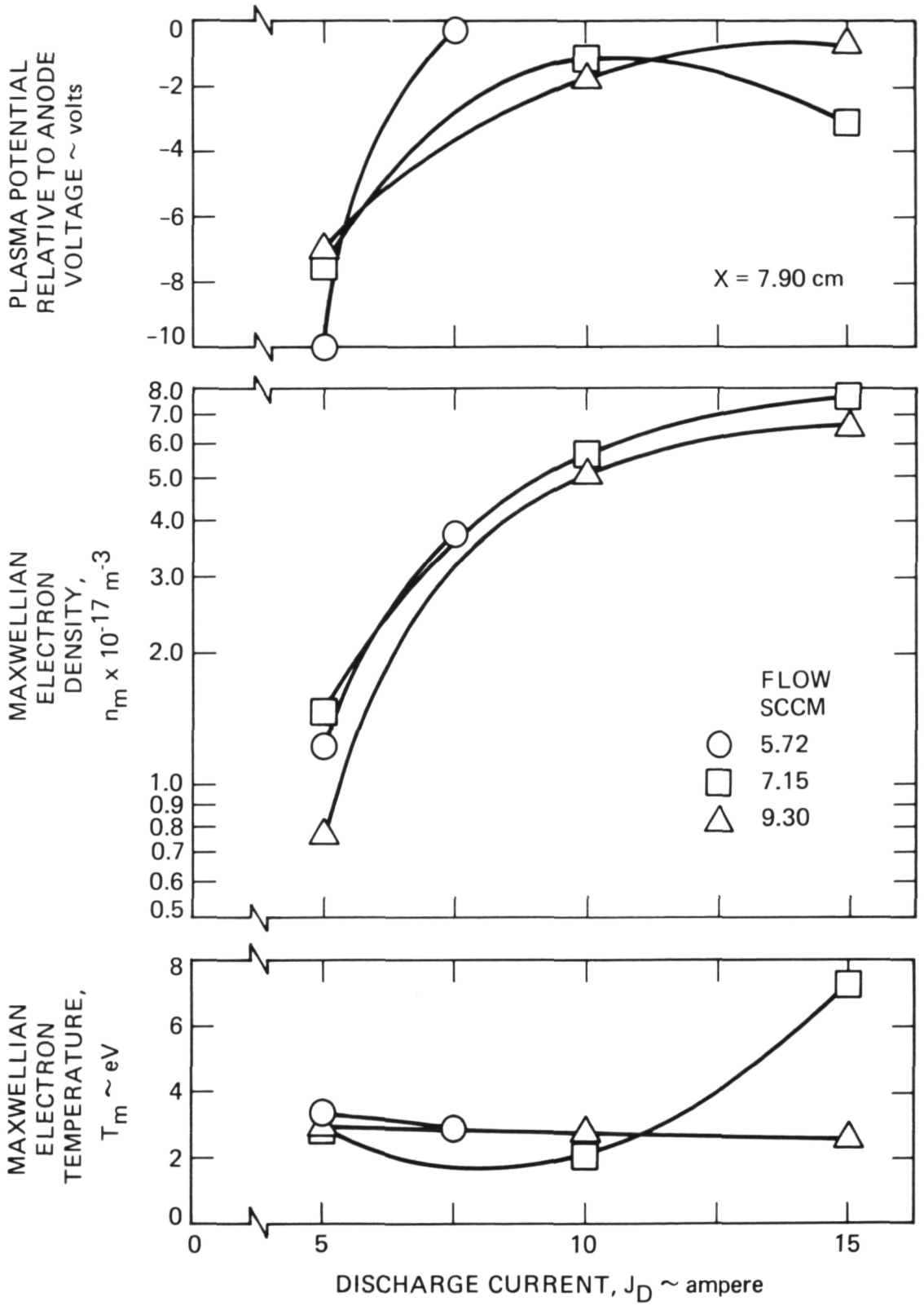

Fig. 22. TBI Engine Discharge Plasma Characteristics: x = 7.90 cm

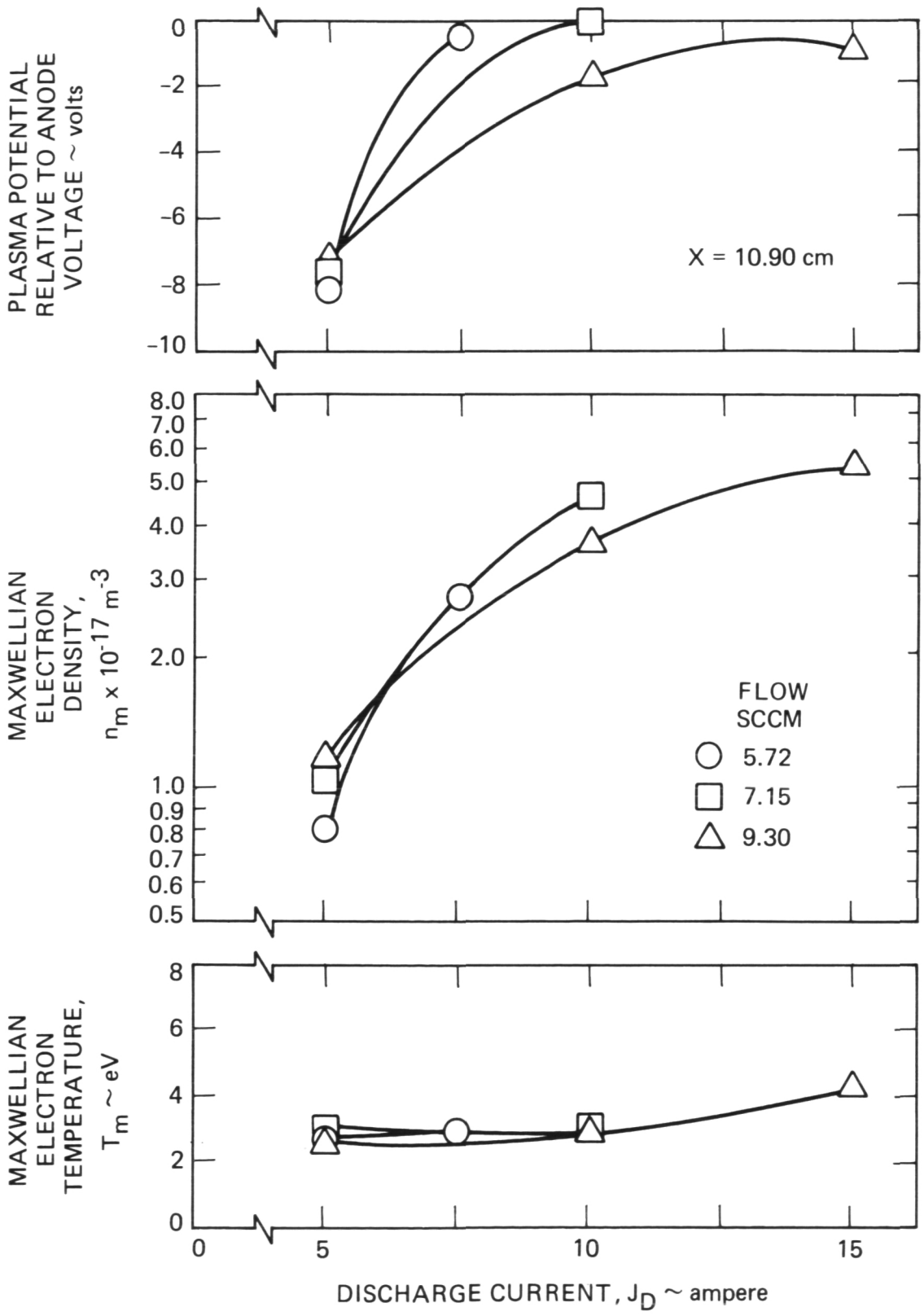

Fig. 23. TBI Engine Discharge Plasma Characteristics: x = 10.90 cm

always negative, relative to anode potential, with two modes of engine operation evident. At low discharge currents, plasma potential was negative of anode potential by 8-10 volts and this difference decreased to about 1-2 volts, negative, with increasing discharge current (it should be noted that the actual value of the anode potential can be found by referring to the V-I curves in Fig. 19). The swiftness of this mode change decreased with increasing propellant flow (or increasing discharge chamber neutral number density). A rapid increase in plasma density accompanied this mode change while electron temperature remained generally unchanged. The low electron temperatures measured are evidence of efficient electron containment within the DLC discharge chamber. Goebel[9] has predicted plasma potentials negative, relative to anode potential, for low electron temperatures. Under these conditions, the electron flux to the anode is increased, by an accelerating potential difference, to maintain the anode power supply current level.

Figure 24 shows the variation in plasma properties with axial probe location for two values of the discharge current, one before and one after the mode change, for the lowest propellant flow investigated. Under all conditions tested it was observed that the electron density gradient, from the peak value to the value near the screen grid, always decreased after the mode change occurred. This decrease is evident in Fig. 24 and suggests a more axially diffuse ion production region. Because of the TBI engine diverging shape, this would significantly increase the available anode area. This additional area would satisfy the anode power supply current requirement and prevent the establishment of a negative plasma-to-anode potential difference which would otherwise be required to increase electron arrival rate at the anode. It is clearly evident, from Fig. 24, that while plasma potentials can be several

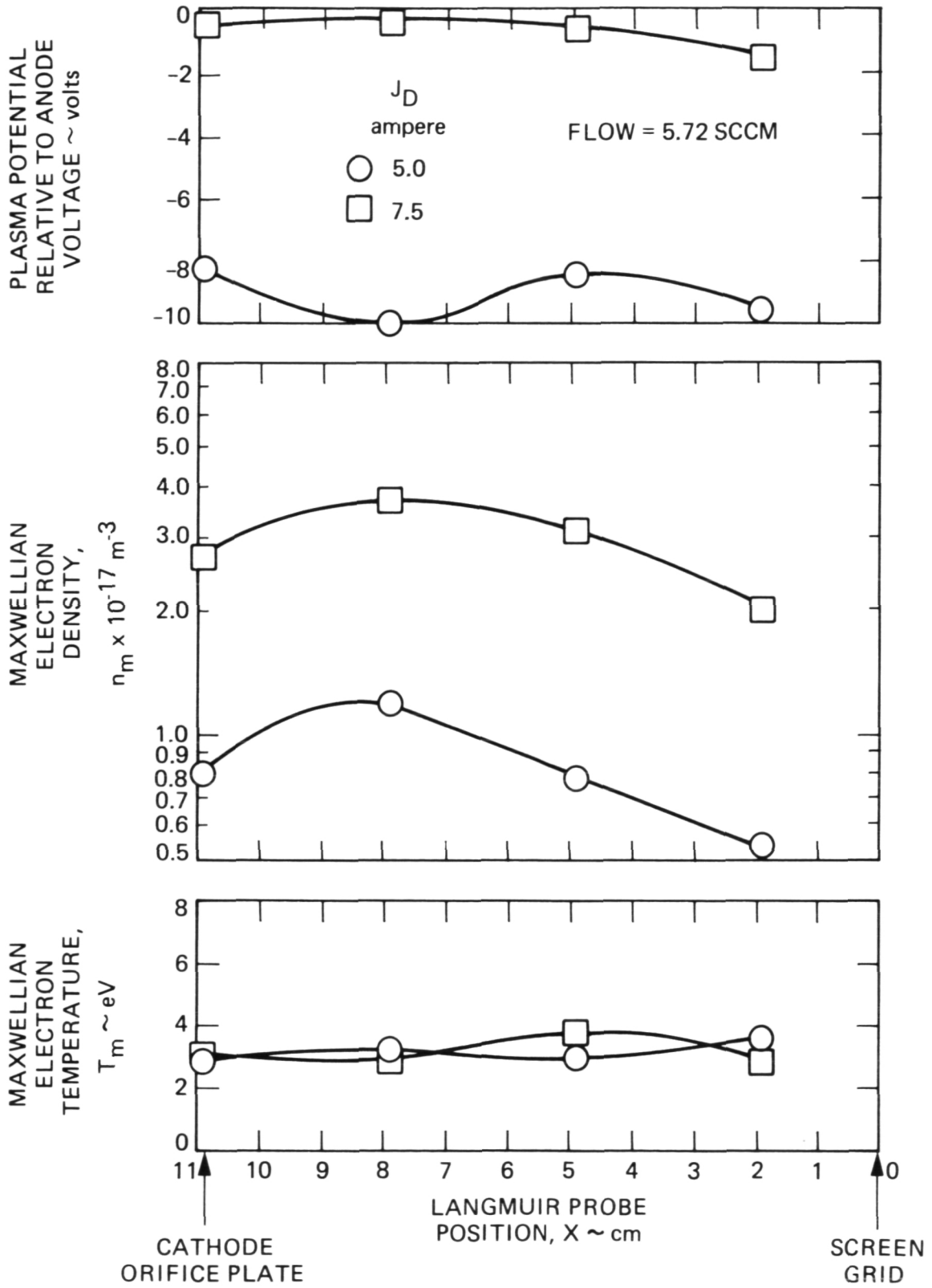

Fig. 24. TBI Engine Mode Change Behavior

volts negative of anode potential, with the TBI engine, much more efficient operation occurs when the plasma potential and anode potential are more equal. The merit of this mode change effect in the TBI engine can be appreciated by observing, in Fig. 24, that a 50% discharge current increase resulted in approximately a 300% plasma density increase.

3.3.3 Optics Mask Biasing

The large graphite plate, to which the DE-AC accelerator system module was mounted (Fig. 10), was isolated from the anode biased DLC discharge chamber. Throughout the test program a 50.0 ohm resistor was used to electrically connect this mask to the chamber. This biasing configuration was chosen because it produced the largest extracted ion current densities. To understand why this occurred a series of tests were performed with the mask (and the attached DE-AC module screen grid) biased, in several different ways, to the TBI engine. Table 1 shows the variation in discharge voltage V_D, mask-to-cathode potential difference V_{MC}, plasma potential measured relative to the cathode emitter tube V_p, Maxwellian electron temperature T_e and Maxwellian electron number density n_m, recorded at a Langmuir probe position 3 cm upstream of the screen grid. For these data identical discharge current and propellant flow rates were maintained.

From Table 1 it is clear that biasing the mask through a 50.0 ohm resistor to the anode would result in larger beam currents because the upstream plasma density is greatest. It appears that this configuration allows some of the higher energy plasma electrons to approach closer to the mask and so increase ion production in this region. By contrast, with the mask acting directly as another anode there is a large electron loss rate to the mask surface. This is evidenced by a plasma potential which becomes

Table 1. Effects of Optics Mask Biasing

Bias Method	V_D (volt)	V_{MC} (volt)	V_P (volt)	T_e (ev)	n_m (m^{-3})
Directly to Cathode	38.9	0	35.7	2.3	2.4×10^{17}
50 ohm to Cathode	39.0	20.9	35.7	2.8	2.5×10^{17}
50 ohm to Anode	37.2	24.1	36.6	2.6	2.9×10^{17}
Directly to Anode	32.4	32.4	36.4	1.9	2.5×10^{17}

positive of anode potential in an effort to curb the loss rate. In addition, the large loss of energetic electrons has depressed the local Maxwellian electron temperature. The small differences noted between the two modes of mask-to-cathode bias are caused by a small electron flux matching the ion flux to the mask in the 50.0 ohm bias configuration. This added electron flux to the mask creates a small increase in ion production and slightly increases electron temperature upstream of the mask. In summary, it is felt that these different optics mask biasing effects may explain why increased beam currents have been observed when ion thruster screen grids have been biased between cathode and anode potential.

3.4 BEAM EXTRACTION CHARACTERISTICS

In conducting the DE-AC accelerator system beam extraction tests, obtaining well documented performance trends was of primary importance. These trends would then serve as a technology base for further DE-AC grid system designs. To this end tests were performed on the impingement variation,

extracted current density scaling behavior and beam divergence characteristics of the DE-AC accelerator system.

3.4.1 Test DE-AC Module Design

The small DE-AC accelerator system module tested during this program is shown, in Fig. 25, positioned in the center of the large graphite plate used to mask down the TBI engine discharge chamber. A hexagonal array pattern of 65 holes, each 1.905 mm in diameter, were match drilled normal to the curved screen and focusing grid surfaces. An upstream center-to-center hole spacing of 2.362 mm was used on the screen grid for an open area fraction of 0.59. Depending on the screen grid radius of curvature, the open area fractions of the downstream screen grid face and upstream and downstream focusing grid faces were successively larger. Both the screen and focusing grids were machined, using conventional milling techniques, from graphite plate stock. Early in the test program several complicated geometries, of both the accelerator and decelerator electrodes, were investigated. However, superior performance (i.e., lowest ion impingement and best beam quality) was achieved by using the simple stainless steel rod design shown in Fig. 25. The insulator mounting arrangements, shown in Fig. 25, were used because they permitted easy DE-AC grid system geometry changes.

3.4.2 Electrode Impingement Current

Figure 26 shows the impingement current variation for the focus, accelerator and decelerator electrodes, of the DE-AC accelerator system, as a function of screen grid voltage. For these data the TBI engine discharge current and voltage were held constant at 15.0 amperes and 41.0 volts respectively. The rapid rise in accelerator grid current at lower screen grid

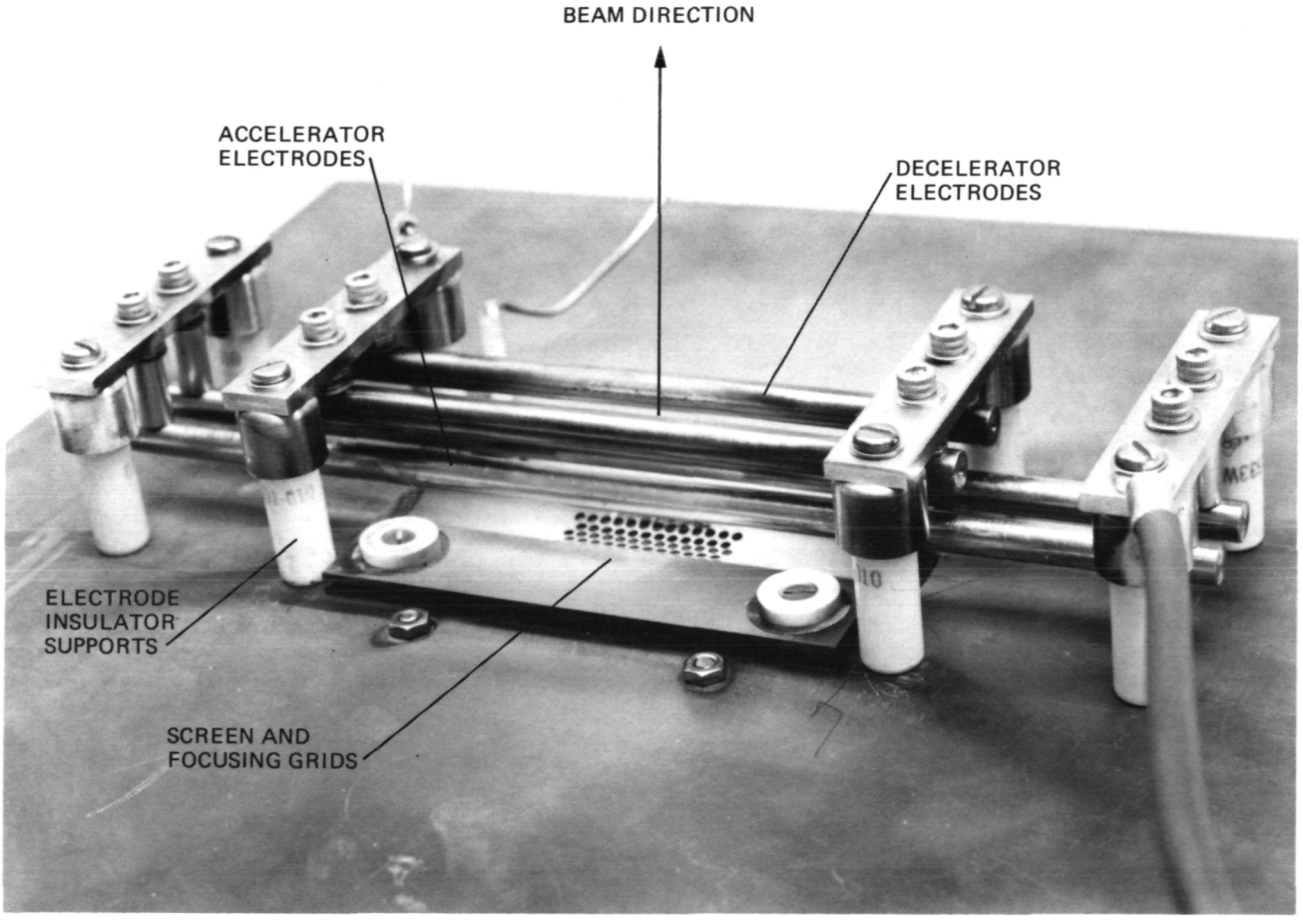

Fig. 25. DE-AC Accelerator System Test Module

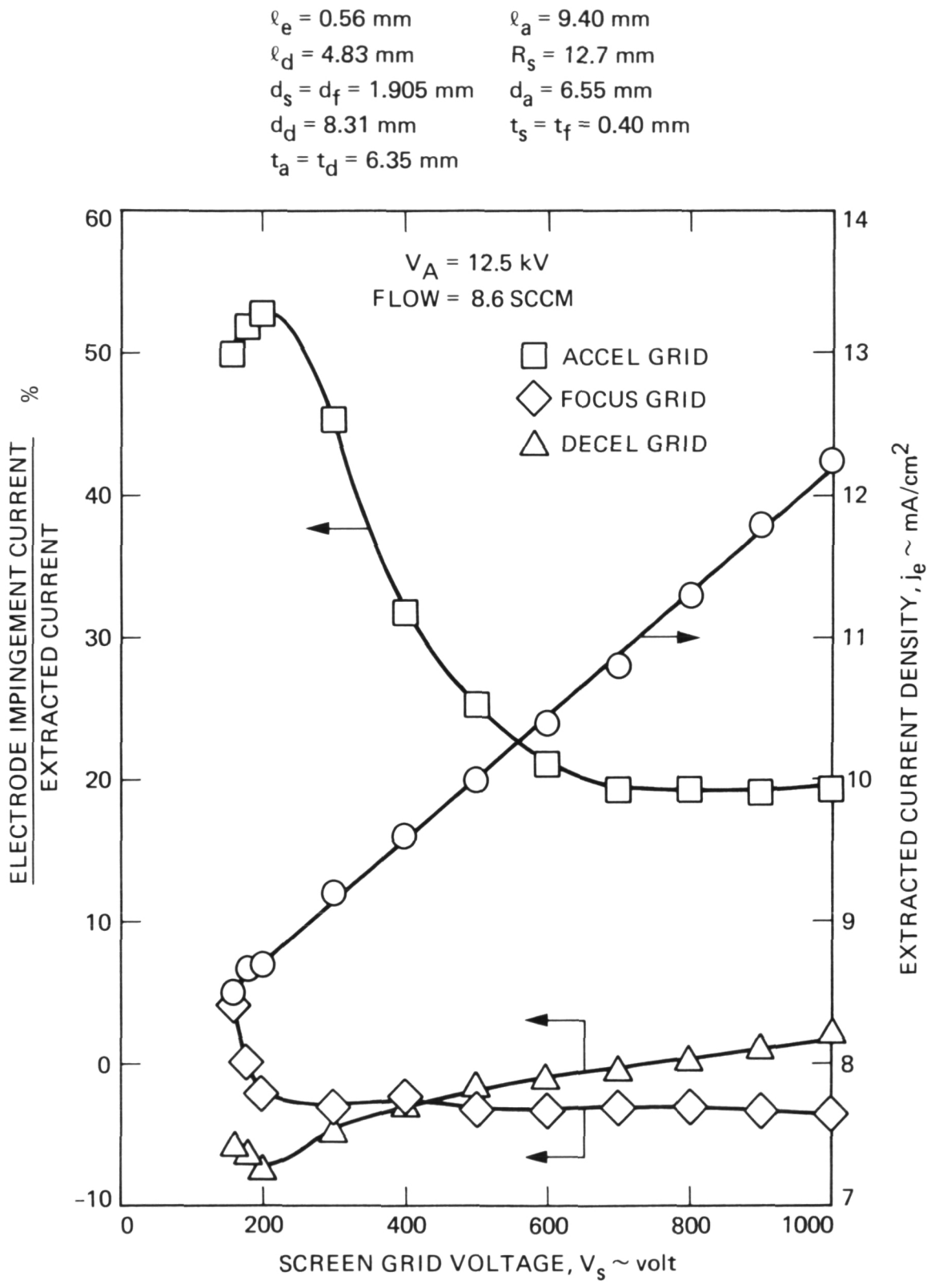

Fig. 26. Effect of Screen Grid Voltage on Impingement

potentials indicates direct ion impingement. This behavior shows that the energy and trajectory of the ions leaving the extraction region are important in ensuring proper ion collimation in the acceleration section. The increased impingement current at low screen voltages, with the focusing and decelerator electrodes, is direct ion impingement. This results from space charge blow up in these regions because of the high current density and low ion velocity.

Good DE-AC grid system operation was achieved with a screen grid radius of curvature that was centered within the accelerator electrode. Three extraction grid sets were tested with the screen grid radius of curvature having values of R_s = 1.27, 1.91 and 3.81 cm but using the same module width, w, and multiple hole pattern. The lowest impingement currents, best beam quality and highest beam currents were obtained with R_s = 1.27 cm. The onset of direct accelerator electrode ion impingement, for a given extracted current density, was very sensitive to the screen grid radius of curvature. It was felt that much lower impingement currents could have been obtained with a screen grid radius of curvature less than 1.27 cm. Time and resources fixed R_s at 1.27 cm in order that the DE-AC module extraction stage characteristics could be adequately investigated. The other DE-AC grid system geometrical parameters noted in Fig. 26 were easier to select than the screen grid radius of curvature and are close to their optimum values. The extraction gap length, ℓ_e, was set at 0.56 mm throughout the test program.

For all beam extraction tests described in this report the baseline impingement currents were very high because of a large neutral gas flow through the accelerator system. This behavior was a result of performing beam extraction tests with a masked down discharge chamber. Because the FERM cathode requires a minimum gas flow to operate (3-5 sccm) the gas flow rate through the 1.8 cm^2 DE-AC module was always very high. As an example, for

the results presented in Fig. 26, the milliampere equivalent neutral flow rate was 32 times the ion current extracted from the plasma. Calculations showed that the charge exchange ion current, created by this excess gas flow, accounted for the large baseline accelerator electrode impingement current shown in Fig. 26. Similarly, the negative focusing and decelerator grid currents were secondary electrons, created by this large charge exchange ion flux, bombarding the accelerator electrode.

3.4.3 Extracted Ion Current Density

Figure 27 shows how post acceleration of the ions results in higher extracted ion current densities for a given extraction gap field stress. These data were obtained by operating the TBI engine at a constant discharge current and voltage and by reducing the screen grid potential while monitoring the change in focusing grid impingement current. The knee of the impingement curves, obtained in this way, defined the onset of space charge blow up and were used to determine the field stress values recorded in Fig. 27. These field stress values were calculated by dividing the screen grid potential by the extraction gap length ℓ_e. Similarly, the values of extracted current density were calculated by dividing the observed screen grid current by the combined area of the 65 screen grid holes in the DE-AC accelerator system test module.

The data curves in Fig. 27 follow a trend where the extracted current density varies approximately as $E_e^{3/2}$ for all V_A values. Typically, post accelerating the ions to 12.5 kV requires about 55% of the extraction gap field stress that would be required by a conventional ion thruster accelerator system, with no post acceleration (V_A=0), to extract a given current density. If an extraction gap field stress, E_e, of 2000V/mm

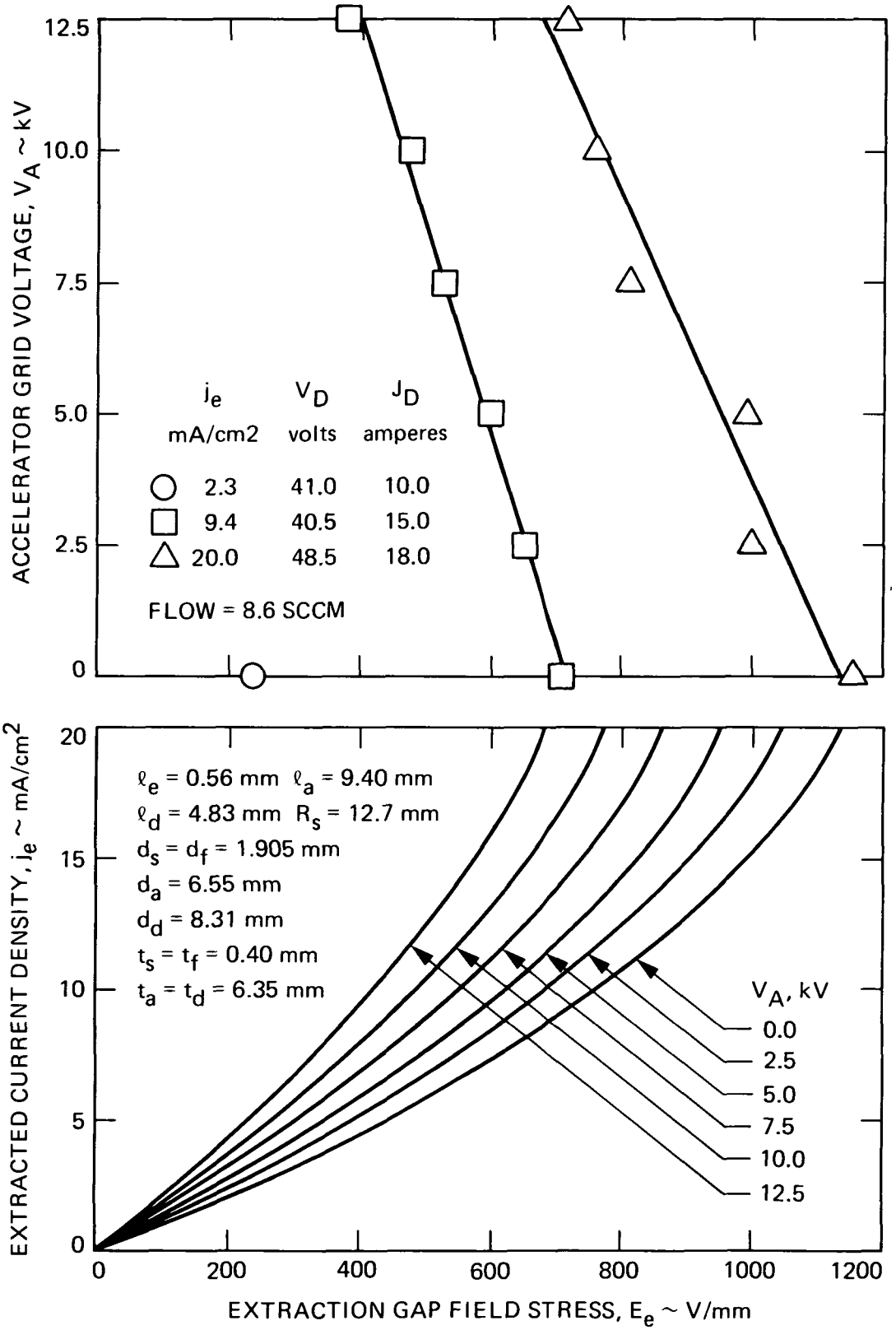

Fig. 27. Effect of Post Acceleration on Extracted Ion Current Density

is assumed for the DE-AC accelerator system, projecting the data trends of Fig. 27 shows that an extracted current density of 100 mA/cm^2, for argon, could be realized with V_A=12.5 kV. Including a conservative screen grid open area fraction of 0.6, the projected beam current density would still be 60 mA/cm^2. The open area fraction for the DE-AC accelerator system may have an effective value much larger than 0.6. This is because the curved screen grid surface (Fig. 2) presents an ion extraction area to the discharge plasma that is larger than the area inferred by the module width, W. The largest electric field stress region in the DE-AC accelerator system, at these high current densities, is the deceleration region where the post accelerated ions are returned to an energy equal to the sum of the screen grid and plasma potential. However, the rod or tubular design of the accelerator and decelerator electrodes permits reliable decelerator gap operation at field stress levels considerably in excess of the extraction gap field stress.

Results for a maximum extracted ion current density of 20 ma/cm^2 are shown in Fig. 27. Arc breakdowns between the shadow shields and metallic (sputter) coated accelerator electrode support insulators (Fig. 25) prevented attainment of higher extracted current densities. The high baseline fraction of accelerator electrode ion impingement, discussed earlier, created a constant source of sputtered material that rapidly coated nearby insulator surfaces. Since this problem was unavoidable, the most intensive data collection was at lower extracted current density levels to ensure that the DE-AC accelerator system performance would be well characterized. From voltage handling, X-ray limits and insulator size considerations, it was felt that the accelerator electrode voltage should not exceed about 15 kV. Taking this as a limit, the required accelerator and decelerator gap field stress

increases, to handle a 100 mA/cm^2 extracted current density, could be realized by reducing the overall DE-AC accelerator system size.

3.5 DE-AC MODULE BEAM QUALITY

3.5.1 Divergence Characteristics

Ion beam quality for the DE-AC accelerator system, shown previously in Fig. 25, was generally good. Faraday probe ion current plots of the beam taken 29 cm downstream from the DE-AC grid module in both the x and y directions, are shown in Fig. 28. For these traces the measured x and y beam divergence angles were 14.0^{o} and 18.0^{o}, respectively. The larger beam spread in the y direction is primarily a result of using open slot accelerator and decelerator electrodes which do not terminate the electric field lines in this direction. With this configuration, ion space charge forces spread the beam as it passes through these electrode gaps. Electrodes were built with bounded slots and beam spreading, in the y direction, was reduced considerably. However, the versatility of the open slot structure, shown in Fig. 25, in terms of being able to alter the electrode slot width, favored its use throughout most of this test program.

For a given extracted ion current density and post acceleration voltage, there was an extraction gap voltage (i.e. screen grid potential) which minimized beam divergence. Similarly, at a fixed screen grid voltage and extracted current density there was an accelerator electrode potential which miminized beam divergence. With the screen and accelerator grid potentials fixed, extracted ion current density variations did not substantially alter the ion beam divergence. This latter behavior was not

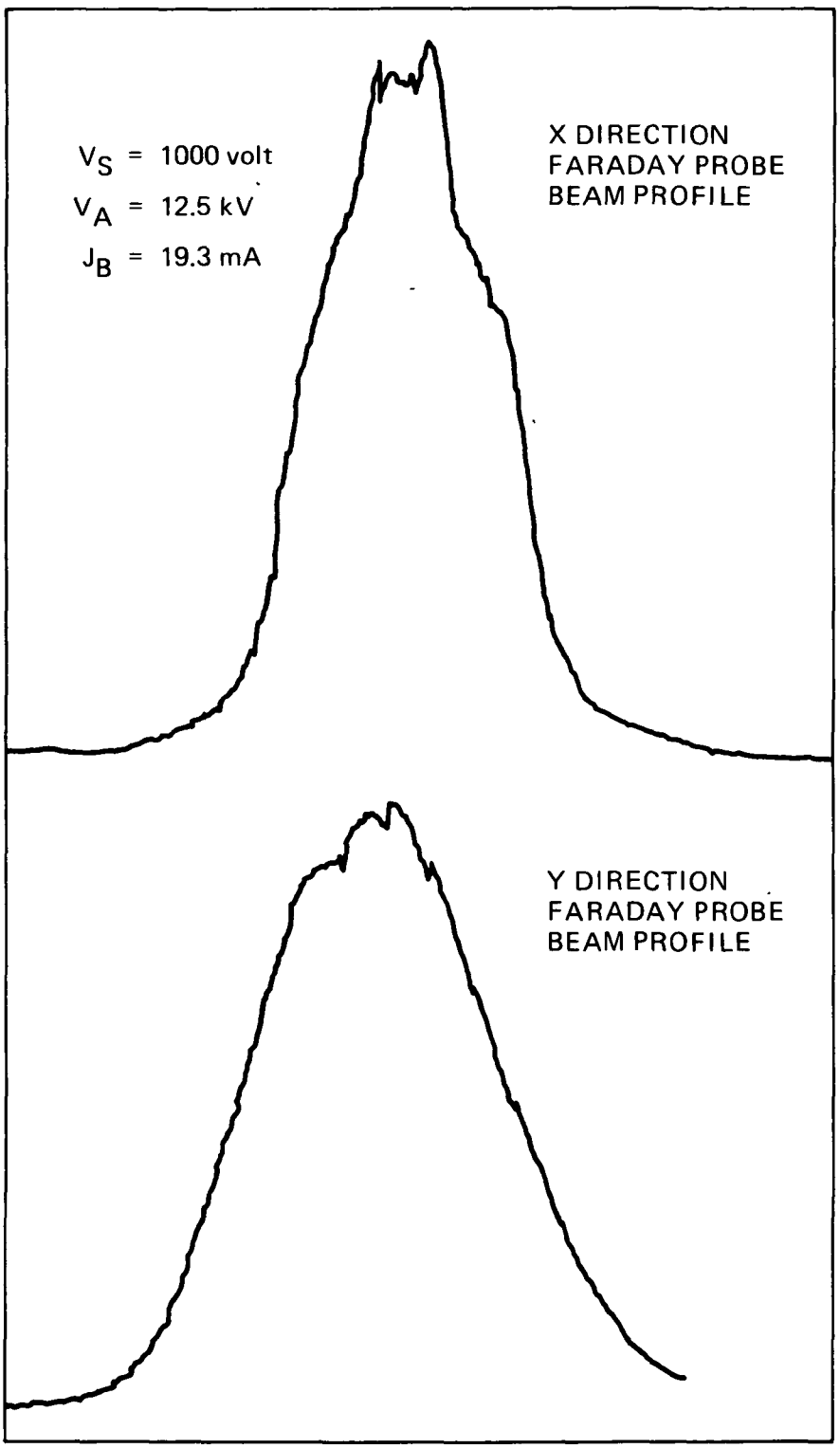

Fig. 28. Beam Profiles Used in Beam Divergence Determinations

true if either the extraction, post acceleration or deceleration gaps, in the DE-AC grid system, were operated close to their perveance limits.

3.5.2 Beam Current Analysis

Integrated beam current was an important parameter in evaluating the performance of the DE-AC accelerator system because both the screen and accelerator electrode power supplies were chassis grounded at their common voltage. This prevented a single meter reading of beam current. Instead, a metered beam current was determined by subtracting the monitored focusing, accelerator and decelerator impingement currents from the recorded screen current. The Farady probe and x-y carriage, described previously, were used to determine the ion beam current distribution. A complete set of beam profiles is shown in Fig. 29 for a given DE-AC grid system operating condition. Each profile was generated by sweeping the probe in the x direction at different y ordinate values. As a result, horizontal displacement, in Fig. 29, corresponds to motion along the x axis while vertical displacement records the collected beam current. The numerical computation of a volume integral, given a closed surface, is a well known process and a computer program was written to carry out this computation. The analysis used linear interpolation between adjoining beam profiles to generate the closed surface of the volume. The base of the volume corresponded to the x-y probe carriage sweep area which measured 30.0 cm by 56.8 cm. A step size of 1 cm was used for incrementing in the x and y directions and was based on the probe area of 1.0 cm^2. The total integrated beam current was the cumulative current contributions from each increment.

Typical input and output of the beam analysis program is reproduced in Fig. 30 for the 9 beam traces shown in Fig. 29. The result of this

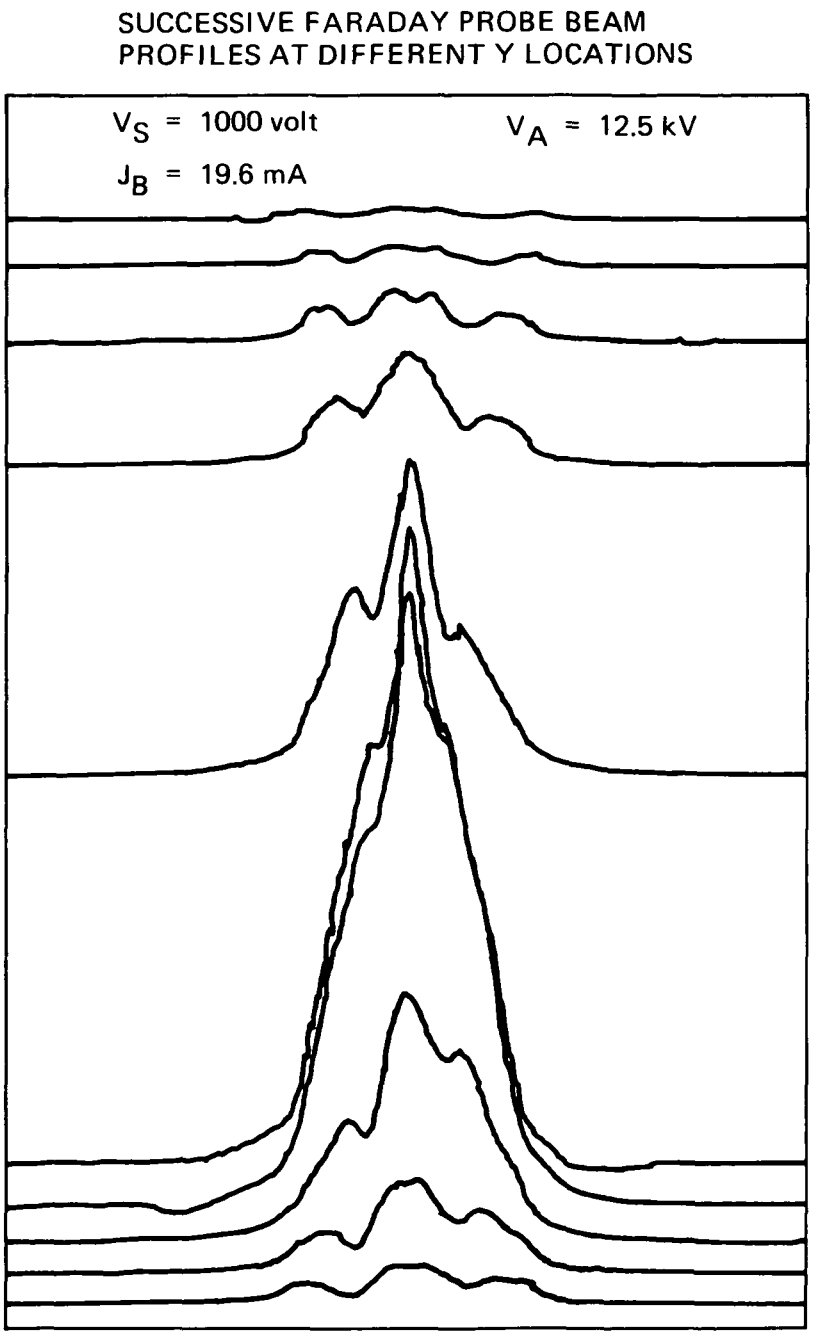

Fig. 29. Complete Beam Scan for Integrated Beam Current Calculations

```
Run option  5 chosen
Z-values in microamps, X- and Y-values in cm

      numcurve *    1      2      3      4      5      6      7      8      9
---------------*-------------------------------------------------------------
      yvalues  *   0.00   3.43   7.00  10.57  14.14  17.71  21.28  24.85  30.00
*****************************************************************************
 curve      X   *
points   values *     Z      -      v      a      l      u      e      s
   1      0.00   *   0.00   0.00   0.00   0.00   0.00   0.00   0.00   0.00   0.00
   2     19.72   *   0.00   0.00   0.00   0.00   0.00   0.00   0.00   0.00   0.00
   3     24.60   *   0.60   1.00   2.00   3.60   0.80   1.80   1.20   0.80   0.20
   4     25.66   *   1.40   2.60   3.80   6.60   3.20   3.20   1.60   1.40   1.20
   5     26.71   *   4.00   6.40   8.00  11.20   8.00   5.20   4.60   3.40   0.80
   6     27.77   *   4.40   9.00  14.00  25.00  20.00  11.00   7.40   4.40   0.20
   7     28.82   *   4.00  10.00  20.40  14.20  38.00  15.60   8.00   4.00   0.20
   8     29.88   *   3.60   9.40  30.00  58.00  49.60  22.00   6.40   2.40   0.80
   9     30.93   *   4.80   9.60  30.00  74.00  68.00  22.00   8.00   3.80   1.40
  10     31.99   *   6.00  13.20  32.00  80.00  79.00  31.00  14.00   8.00   1.60
  11     33.04   *   6.40  15.40  39.00  96.00100.00  49.00  17.60   6.40   1.40
  12     34.10   *   6.60  14.20  36.80  78.00  75.00  42.00  17.00   8.00   2.00
  13     35.15   *   3.60   9.00  22.00  62.80  68.00  26.00  12.00   7.00   1.80
  14     36.21   *   2.00   4.00  18.40  56.50  60.00  29.00   9.00   3.40   0.80
  15     37.26   *   2.20   6.40  18.00  44.80  47.00  26.60  10.80  '4.00   0.20
  16     38.32   *   3.20   6.60  12.60  30.00  32.00  16.00   9.20   5.60   1.10
  17     39.38   *   3.20   5.00   8.00  15.00  15.00   8.40   5.80   4.60   1.60
  18     40.43   *   1.40   2.20   5.00   7.00   7.00   4.20   2.40   1.60   1.20
  19     41.49   *   0.80   1.40   2.80   3.20   4.00   3.60   1.60   0.80   0.00
  20     45.10   *   0.00   0.40   0.20   0.00   0.60   0.60   0.60   0.00   0.00
  21     56.83   *   0.00   0.00   0.00   0.00   0.00   0.00   0.00   0.00   0.00

*** FINAL RESULT ***
The total collected beam current is 1.0671E-002 amperes.
```

Fig. 30. Sample Output of Integrated Beam Current Program

analysis indicates an integrated beam current of 10.7 mA. The measured beam current, recorded by the metered DE-AC grid system electrodes, for this example was 19.6 mA. Further analysis showed that this factor of two difference in beam current determination was due to ion charge exchange along the beam line. As described in an earlier section, the neutral propellant loss rate through the DE-AC test module was typically 30 times the metered beam current. Charge exchange production rate calculations were performed by modeling this neutral flow stream as a succession of expanding hemispherical shells and also by a sharp-edged orifice, neutral density distribution, flow as used by Kaufman[10]. In both cases the calculated beam current, reaching the Faraday probe target plane, had been reduced from 19.6 mA to approximately 13.6 mA. The 25% difference between this result and the measured 10.7 mA is believed attributable to a lesser neutral density drop off along the beam line than was assumed for the calculations. This is believed to result from the large depth of the DE-AC accelerator system (~2 cm) and a downstream ground shield shaped like a 3 cm long beam channel, both of which would create a more collimated neutral stream.

SECTION 4

ADVANCED ION ENGINE PERFORMANCE

An argon ion beam current density of 60 mA/cm^2, using the DE-AC accelerator system, appears to be feasible. At this beam current density it becomes possible to seriously contemplate development of a one newton thrust ion engine. In the following analysis, performance levels of such an engine were determined based upon the assumptions listed below:

(i) Ion beam area comparable to a 30-cm J series thruster, 625 cm^2, with a beam flatness parameter of 1.0

(ii) Use of a FERM hollow cathode, in the self heating mode, for the main and neutralizer cathodes, with no heater, vaporizer, or keeper, power supplies.

(iii) DE-AC accelerator system extraction gap field stress of 2000 V/mm.

Ion engine performance was described by the following set of equations.

Thrust, T:

$$T = \frac{J_B m g I_{sp}}{e \eta_u} \quad .$$

Total Power, P:

$$P = J_B \left[\frac{m}{2e} \left(\frac{g I_{sp}}{\eta_u \gamma} \right)^2 + \varepsilon + V_{NC} \right] \quad .$$

Thruster Efficiency, η_T:

$$\eta_T = \frac{\gamma^2 \eta_u}{1 + \frac{2e}{m}\left(\frac{\eta_u \gamma}{g I_{sp}}\right)^2 \left[\varepsilon + V_{NC}\right]}$$

The solutions of these equations for a constant thrust, T = 1.0 newton, are presented in Table 2 as a function of discharge loss ε.

Table 2: One Newton Ion Engine Performance

ε (eV/ion)	J_B (ampere)	I_{sp} (secs.)	T (newton)	P (watts)	η_T
Argon, assumes γ = 0.95, η_u = 0.90, V_{NC} = 30 volt					
100	37.5	5860	1.000	40191	0.713
80	37.5	5860	1.000	39441	0.727
60	37.5	5860	1.000	38691	0.741
Xenon, assumes γ = 0.95, η_u = 0.95, V_{NC} = 15 volt					
100	20.3	3340	1.000	21426	0.764
80	20.3	3340	1.000	21020	0.779
60	20.3	3340	1.000	20613	0.794
Mercury, assumes γ = 0.95, η_u = 0.97, V_{NC} = 12 volt					
100	16.8	2815	1.000	17628	0.782
80	16.8	2815	1.000	17292	0.797
60	16.8	2815	1.000	16956	0.813

Table 2 shows clearly the power penalty in using a light atomic weight propellant, such as argon, in a high thrust density ion engine. Mercury, because of the superior performance afforded by its high atomic weight, low ionization potential and minimal storage requirements, is the preferred propellant for interplanetary propulsion. The major technical challenges associated with the development of a one newton thrust mercury ion engine, as defined in Table 2, are listed below:

(i) Design and construction of a full size (625 cm^2) DE-AC accelerator system and demonstration of full power beam extraction for extended periods of time.

(ii) Reliable, long life, hollow cathode operation at 73 amperes emission current (assuming a 100 eV/ion discharge loss) using either a scaled up version of present thruster hollow cathodes or the FERM cathode discussed in this report.

(iii) Development of an efficient discharge chamber whose magnetic field structure provides a beam flatness parameter approaching 1.0

(iv) Passive control of discharge chamber heat loss (estimated to be 2184 watts for a 1.0 newton mercury ion engine) while ensuring that the samarium cobalt magnet temperatures do not exceed the demagnetization limit.

SECTION 5

CONCLUSIONS

A Test Bed Ion (TBI) engine has been developed to serve as a tool in exploring the limits of electrostatic ion thruster performance. A preliminary investigation, using the TBI engine and its component technologies, has shown that substantial thrust density increases may be achieved over present ion thrusters. Principally, these thrust density increases can be realized by using the Decoupled Extraction and Amplified Current (DE-AC) accelerator system. Reduced electric field stress requirements enable this accelerator system to extract very high ion current densities. An argon ion beam current density of 60 mA/cm^2 was shown to be technically feasible.

Tests of a water cooled, Divergent Line Cusp (DLC), discharge chamber have demonstrated that the TBI engine can be operated at discharge powers of several kilowatts without damage to its samarium cobalt permanent magnets. Extensive Langmuir probe characterization, of the plasma generated within the pyramid shaped DLC chamber, identified plasma potentials negative of anode potential. In one engine operating mode, this negative potential difference was as large as 8-10 volts, with low plasma density. In a second mode, with plasma potential 1-2 volts negative of anode potential, very high plasma densities were obtained.

Electron currents of 35 amperes were demonstrated using the Field Enhanced Refractory Metal (FERM) cathode. This simple, rugged device, used a metal tube electron emitter and required no oxide insert resistance heaters. TBI engine start up times, using the FERM cathode, were typically 1-2 secs. In addition, the FERM cathode is easily scaled to higher currents thus making

the TBI engine capable of generating the large plasma densities required to explore the maximum projected beam current levels of the DE-AC accelerator system.

A 1.0 newton thrust ion engine, with beam area comparable to the present J series 30 cm thruster, appears to be a realizable technology goal. This conclusion is based upon the performance projections and component designs of the Test Bed Ion engine, in addition to, reasonable estimates of parameter values not evaluated during this program. Calculations show that such an engine, operating on Xe or Hg propellant, could have thruster efficiencies as high as 0.76 and 0.78, respectively, with a 100 ev/ion discharge loss.

SECTION 6

REFERENCES

1. Aston, G., "High Efficiency Ion Beam Accelerator System," Rev. Sci. Instrum., Vol. 52 No. 9, Sept. 1981, pp. 1325-1327.

2. Aston, G. and Kaufman, H. R., "The Ion-Optics of a Two-Grid Electron-Bombardment Thruster," AIAA Paper No. 76-1029, Nov. 1976.

3. Rovang, D. C. and Wilbur, P. J., "Ion Extraction Capabilities of Very Closely Spaced Grids," AIAA Paper No. 82-1894, Nov. 1982.

4. Seigfried, D., "Studies on an Experimental Quartz Tube Hollow Cathode," AIAA Paper No. 79-2056, Nov. 1979.

5. Meek, J. M. and Craggs, J. D., "Electrical Breakdown of Gases," Oxford University Press, 1953.

6. Sovey, J. S., "Improved Ion Containment Using a Ring Cusp Ion Thruster," AIAA Paper No. 82-1928, Nov. 1982.

7. Poeschel, R. L., "Development of Advanced Inert-Gas Ion Thrusters," NASA CR-168206, July 1983.

8. Beattie, J. R., "Numerical Procedure for Analyzing Langmuir Probe Data," AIAA Journal, Vol. 13, No. 7, July 1975, pp. 950-952.

9. Goebel, D. M., "Ion Source Discharge Performance and Stability," Phys. Fluids, Vol. 25, No. 6, June 1982, pp. 1093-1102.

10. Kaufman, H. R., "Charge-Exchange Plasma Generated by an Ion Thruster," NASA CR-134844, June 1975.

SECTION 7

APPENDIX A

Child's Law with Non-Zero Initial Ion Velocity

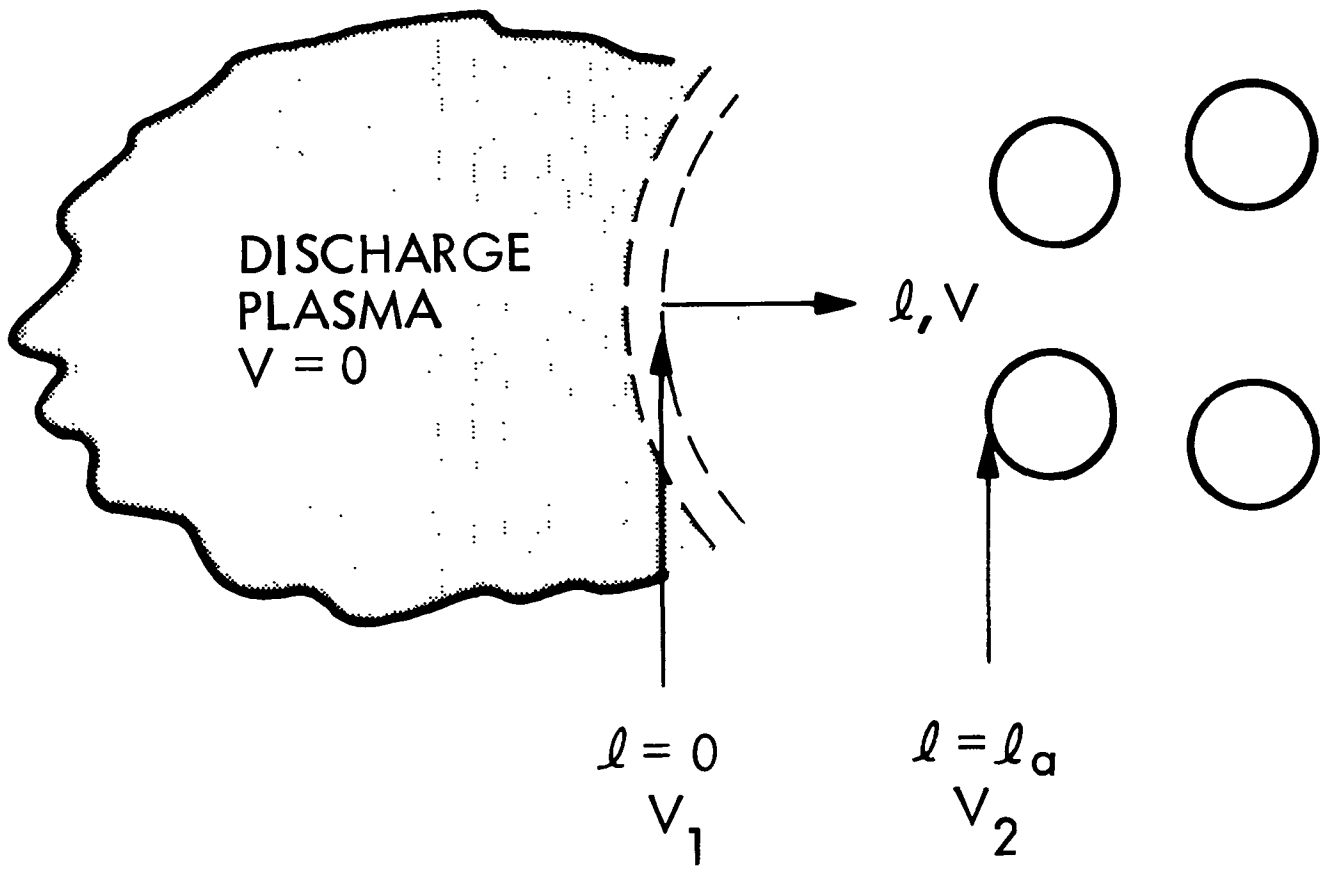

From Poisson's equation in one dimension

$$\frac{d^2V}{d\ell^2} = \frac{\rho}{\varepsilon_o} \quad . \qquad 1$$

Assuming a uniform ion current density, j_A, in the post acceleration section

$$\rho = \frac{j_A}{v} \quad . \qquad 2$$

From energy conservation the ion velocity, v, is

$$v = \left(\frac{2eV}{m}\right)^{\frac{1}{2}} \qquad 3$$

Substituting eqs 1 and 2 into eq. 3 gives

$$\frac{d^2V}{d\ell^2} = \frac{j_A}{\varepsilon_o}\left(\frac{m}{2eV}\right)^{\frac{1}{2}}$$

where ε_o is the vacuum permitivity, m is ion mass and e the electronic charge. Multiplying both sides of this equation by $\frac{dV}{2d\ell}$ and integrating results in

$$\int_o^{\ell} \frac{d}{d\ell}\left(\frac{dV}{d\ell}\right)^2 d\ell = \frac{2j_A}{e_o}\left(\frac{m}{2e}\right)^{\frac{1}{2}} \int_{V_1}^{V} V^{-\frac{1}{2}}\, dV \quad .$$

Since $\frac{dV}{d\ell}$ is small within the focusing grid holes, (ℓ=0), we may approximate by

$$\frac{dV}{d\ell} \approx 2\left(\frac{j_A}{\varepsilon_o}\right)^{\frac{1}{2}} \left(\frac{m}{2e}\right)^{\frac{1}{4}} \left(V^{\frac{1}{2}} - V_1^{\frac{1}{2}}\right)^{\frac{1}{2}} \quad .$$

Further integrating

$$\int_{V_1}^{V_2} \frac{dV}{\left(V^{\frac{1}{2}} - V_1^{\frac{1}{2}}\right)^{\frac{1}{2}}} = 2\left(\frac{j_A}{\varepsilon_o}\right)^{\frac{1}{2}} \left(\frac{m}{2e}\right)^{\frac{1}{4}} \int_o^{\ell_a} d\ell \quad .$$

This becomes

$$2\left(\frac{2}{3}\left(V_2^{\frac{1}{2}} - V_1^{\frac{1}{2}}\right)^{\frac{3}{2}} + 2V_1^{\frac{1}{2}}\left(V_2^{\frac{1}{2}} - V_1^{\frac{1}{2}}\right)^{\frac{1}{2}}\right) = 2\left(\frac{j_A}{\varepsilon_o}\right)^{\frac{1}{2}} \left(\frac{m}{2e}\right)^{\frac{1}{4}} \ell_a \quad .$$

Rearranging the LHS this reduces to

$$\frac{2}{3} V_1^{\frac{3}{4}}\left(\left(\left(\frac{V_2}{V_1}\right)^{\frac{1}{2}} - 1\right)^{\frac{1}{2}} \left(\left(\frac{V_2}{V_1}\right)^{\frac{1}{2}} + 2\right)\right) = \left(\frac{j_A}{\varepsilon_o}\right)^{\frac{1}{2}} \left(\frac{m}{2e}\right)^{\frac{1}{4}} \ell_a \quad .$$

Further manipulation gives

$$j_A = \frac{4}{9}\varepsilon_o \left(\frac{2e}{m}\right)^{\frac{1}{2}} \frac{V_2^{\frac{3}{2}}}{\ell_a^2} \frac{\left(\left(\frac{V_2}{V_1}\right)^{\frac{1}{2}} - 1\right)\left(\left(\frac{V_2}{V_1}\right)^{\frac{1}{2}} + 2\right)^2}{\left(\frac{V_2}{V_1}\right)^{\frac{3}{2}}} \quad .$$

Setting j_{AO} as the usual Child's Law current density the effect of a non-zero initial ion velocity is to increase this current density by the ratio

$$\frac{j_A}{j_{AO}} = \frac{\left(\left(\frac{V_2}{V_1}\right)^{\frac{1}{2}} - 1\right)\left(\left(\frac{V_2}{V_1}\right)^{\frac{1}{2}} + 2\right)^2}{\left(\frac{V_2}{V_1}\right)^{\frac{3}{2}}}$$

Where, in terms of familiar DE-AC electrode potentials, measured with respect to facility ground, $V_1 = V_s - V_f$ and $V_2 = |V_A| + V_s$.

DISTRIBUTION LIST

	Copies
National Aeronautics and Space Administration Washington, DC 20546	
Attn: MP-3/Mr. Ivan Bekey	1
RSE-5/Mr. David Byers	1
RTS-6/Mr. Jerome Mullin	1
National Aeronautics and Space Administration Lewis Research Center 21000 Brookpark Road Cleveland, OH 44135	
Attn: Research Support Procurement Section	
Mr. Don Hoffman, MS 500-305	1
Technology Utilization Office, MS 3-19	1
Report Control Office, MS 5-5	1
Library, MS 60-3	2
Mr. N. Musial, MS 500-113	1
Dr. M. Goldstein, Chief Scientist, MS 5-3	1
Mr. T. Cochran, MS 501-5	1
Mr. F. Terdan, MS 501-7	1
Mr. V. Rawlin, MS 501-7	20
National Aeronautics and Space Administration Marshall Space Flight Center Huntsville, AL 35812	
Attn: Mr. Robert Bechtel	1
Research and Technology Division Wright-Patterson AFB, OH 45433	
Attn: (ADTN) Mr. Everett Bailey	1
NASA Scientific and Technical Information Facility P.O. Box 8757 Blatimore, MD 21240	
Attn: Accessioning Dept.	1
DST 1 Ministry of Defence Metropole Building Northumberland Avenue London, WC2 N5BL ENGLAND	
Attn: Dr. D. G. Fearn	1

	Copies
National Aeronautics and Space Administration Goddard Space Flight Center Greenbelt, MD 20771 Attn: Dr. David H. Suddreth	1
COMSAT Laboratories P.O. Box 115 Clarksburg, MD 20734 Attn: Mr. B. Free	1
Intelsat 490 L'Enfant Plaza, S.W. Washington, DC 20024 Attn: Mr. Rolland Schreib	1
Rocket Propulsion Laboratory Edwards AFB, CA 93523 Attn: LKDH/Mr. Frank Meade LKDH/Capt. Elledge LKDH/Dr. R. Vondra	1 1 2
Giessen University 1st Institute of Physics Giessen, West Germany Attn: Professor H. W. Loeb	1
Jet Propulsion Laboratory 4800 Oak Grove Drive Pasadena, California 91109 Attn: Technical Library Mr. W. Gin Mr. J. Stocky Dr. G. Aston Dr. D. King Mr. T. Divirotto Mr. W. Deininger Mr. C. Garner Mr. E. Pawlik Mr. R. Jones Mr. K. Nock	1 1 1 1 1 1 1 1 1 1 1
Electro-Optical Systems, Inc. 300 North Halstead Pasadena, California 91107 Attn: Mr. E. James Mr. W. Ramsey	1 1

	Copies
TRW Inc. TRW Systems One Space Park Redondo Beach, California 90278 Attn: Mr. Sid Zafran	1
National Aeronautics and Space Administration Ames Research Center Moffett Field, California 94035 Attn: Technical Library	1
National Aeronautics and Space Administration Langley Research Center Langley Field Station Hampton, Virginia 23365 Attn: Technical Library	1
Hughes Research Laboratories 3011 Malibu Canyon Road Malibu, California 90265 Attn: Mr. J. H. Molitor Dr. R. L. Poeschel Dr. Jay Hyman Dr. J. R. Beattie Dr. W. S. Williamson Dr. H. J. King	 1 1 1 1 1 1
Princeton University Princeton, NJ 08540 Attn: Dean R. G. Jahn Dr. Arnold Kelly	 1 1
Boeing Aerospace Co. P.O. Box 3999 Seattle, Washington 98124 Attn: Mr. Donal Grim, MS 8K31	 1
Electrotechnical Laboratory 1-1-4, Umezono, Sakura-Mura, Niihari-Gun Ibaraki, JAPAN Attn: Dr. Katsuya Nakayama	 1
Michigan State University East Lansing, MI 48824 Attn: Dr. J. Asmussen Dr. M. C. Hawley	 1 1

	Copies
The Aerospace Corporation Space Sciences Lab. P.O. Box 92957 Los Angeles, California 90009 Attn: Mr. T. Silva	1
Department of Aeronautics Faculty of Engineering University of Tokyo 7-3-1, Hongo, Bunkyo-ku Tokyo, JAPAN Attn: Prof. Itsuro Kimura	1
Dr. Pradosh Ray Tuskegee Institute School of Engineering Tuskegee Institute, AL 36088	1
Dr. Chris Olson Dept. Of Physics University of Huntsville Huntsville, AL 35899	1
Dr. Kevin Rudolph MS. M0482 Martin Marietta Aerospace P.O. Box 179 Denver, CO 80201	1
Dr. Rolf Buhler Institut Fur Raumfahrtantriebe Universitat Stuttgart 7 Stuttgart 80 Pfaftenwaldring 31 West Germany	1
Colorado State University Fort Collins, CO 80523 Attn: Dr. H. R. Kaufman Dr. R. S. Robinson Dr. P. J. Wilbur	1 1 1
Dr. David Finkelstein Dept. of Physics Georgia Institute of Technology Atlanta, GA 30332	1